iScience

CellPress
OPEN ACCESS

Article

Crystal engineering of high explosives through lone pair-π interactions: Insights for improving thermal safety

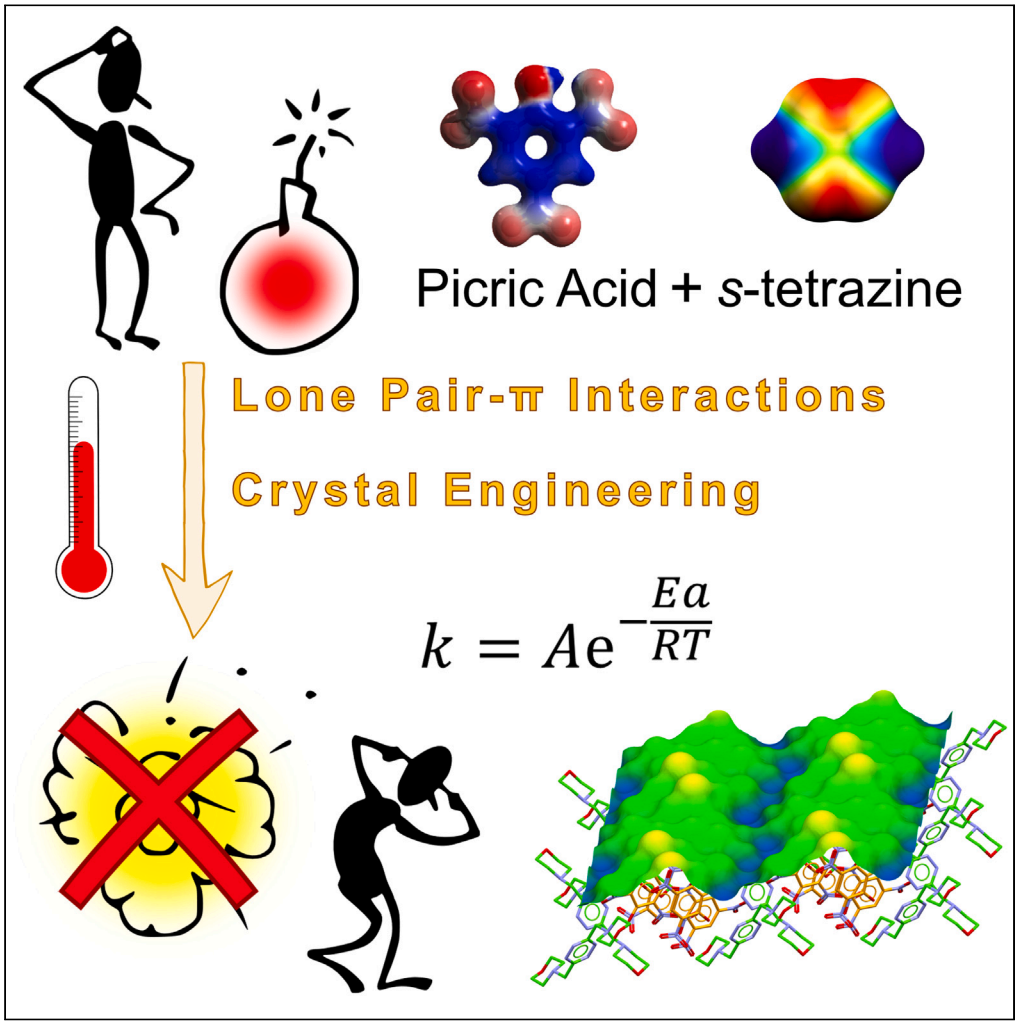

Matteo Savastano, María Dolores López de la Torre, Marco Pagliai, ..., Carla Bazzicalupi, Manuel Melguizo, Antonio Bianchi

matteo.savastano@uniroma5.it (M.S.)
carla.bazzicalupi@unifi.it (C.B.)
mmelgui@ujaen.es (M.M.)

Highlights

s-tetrazine can be exploited for anion-π, π-π or lone pair-π interactions at will

High-energy density s-tetrazine-based ligands/picric acid complexes were prepared

Experimental thermokinetic parameters correlate with intermolecular contacts

Safety of high-explosives can be improved through crystal engineering

Savastano et al., iScience *26*, 107330
September 15, 2023
https://doi.org/10.1016/j.isci.2023.107330

iScience

CellPress
OPEN ACCESS

Article

Crystal engineering of high explosives through lone pair-π interactions: Insights for improving thermal safety

Matteo Savastano,[1,2,6,*] María Dolores López de la Torre,[3] Marco Pagliai,[2] Giovanna Poggi,[2,4] Francesca Ridi,[2,4] Carla Bazzicalupi,[2,*] Manuel Melguizo,[3,*] and Antonio Bianchi[2,5]

SUMMARY

In this high-risk/high-reward study, we prepared complexes of a high explosive anion (picrate) with potentially explosive *s*-tetrazine-based ligands with the sole purpose of advancing the understanding of one of the weakest supramolecular forces: the lone pair-π interaction. This is a proof-of-concept study showing how lone pair-π contacts can be effectively used in crystal engineering, even of high explosives, and how the supramolecular architecture of the resulting crystalline phases influences their experimental thermokinetic properties. Herein we present XRD structures of 4 novel detonating compounds, all showcasing lone pair-π interactions, their thermal characterization (DSC, TGA), including the correlation of experimental thermokinetic parameters with crystal packing, and *in silico* explosion properties. This last aspect is relevant for improving the safety of high-energy materials.

INTRODUCTION

The *s*-tetrazine moiety has a wide range of properties which made it attractive for several different purposes. First, being an H,C,N-containing planar molecule with high N/C ratio, it is easily identified as an aromatic of choice for the development of high-energy materials, explosives, and pyrotechnics.[1,2] This does not exhaust *s*-tetrazine applications in material chemistry since it possesses a ring-centred π* lowest unoccupied molecular orbital (LUMO) and generally gives rise to reversible redox processes, making it appealing for new materials for energy storage,[3] oxidation photocatalysts,[4–6] polymer biosensors,[7,8] or molecular magnets[9,10] built from metal complexes of tetrazine anion radicals. It also finds applications as 2,3 diazadiene in inverse electron-demand Diels Alder reactions, making it attractive for organic synthesis[11] and metal-free biorthogonal chemistry[12,13] as well as the recently proposed photocatalytically activated orthogonal chemistry[14] that enable subcellular biomolecular labeling applications in living systems. Lastly, its extreme (in the sense that azines with more than 4 N atoms are not stable) polarization and positive Q_{zz} quadrupolar moment[15] make it an attractive moiety for anion coordination chemistry as it gives rise to strong anion-π interactions,[16–18] which have also been exploited for anion signaling[19] and anion-driven self-assembly[20–22] or as part of macrocyclic ligands intended for hosting anions.[23,24]

We have previously investigated the anion-binding properties of a series of symmetrical morpholine derivatives, L1-L4, Figure 1, possessing spacers of different length (Lx, x = 1–4, where x = number of $-CH_2-$ in-between morpholine and *s*-tetrazine moieties). A large collection of evidence, including aqueous solution (potentiometry, ITC, DOSY NMR), solid state (>20 crystal structures), and DFT data, substantiated strong anion-π interactions.[25–29] Cooperativity of anion-morpholinium salt bridges with anion-π interactions can be relevant for shorter derivatives (especially L2), yet all ligands were found to still bind anions even in their not-protonated form and/or when such cooperativity is hindered by excessive spacing out of *s*-tetrazine and morpholinium sites. Mono- and polyatomic inorganic anions were found to always give strong and centered anion-π interactions (Figure 2).[16,25–29] Organic anions have been explored as combinations of carboxylate/sulphonate-type anions of aromatic/aliphatic nature: it was found that the geometry of the charged group affects complex stability and ligand/substrate mutual orientations.[30] In the specific case of flat aromatic and electron-rich carboxylates, carboxylate-morpholinium H-bonds were found, while *s*-tetrazine gives rise to strong π-π interactions with the aromatic portion of the anion (Figure 2).

[1]Department of Human Sciences and Quality of Life Promotion, University San Raffaele Roma, Via di Val Cannuta 247, 00166 Rome, Italy

[2]Department of Chemistry "Ugo Schiff", University of Florence, Via della Lastruccia 3, 50019 Sesto Fiorentino, Italy

[3]Department of Inorganic and Organic Chemistry, University of Jaén, 23071 Jaén, Spain

[4]CSGI, University of Florence, Via della Lastruccia 3, 50019 Sesto Fiorentino (FI), Italy

[5]Senior author

[6]Lead contact

*Correspondence: matteo.savastano@uniroma5.it (M.S.), carla.bazzicalupi@unifi.it (C.B.), mmelgui@ujaen.es (M.M.)

https://doi.org/10.1016/j.isci.2023.107330

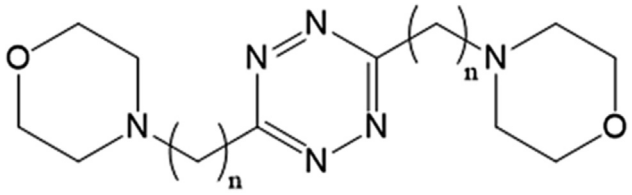

Figure 1. *s*-tetrazine-based ligands addressed in this study

This large body of evidence, together with that concerning the commercial ligand 3,6-di(pyridin-4-yl)-1,2,4,5-tetrazine, also used to stabilize 3D networks through supramolecular interactions with anionic substrates,[31] has led us to present a global view of the usefulness of *s*-tetrazines as binding sites for anions and nucleophilic species in general.[16] On that occasion, relevance of lone pair-π interactions for these systems was first noticed.

Lone pair-π interactions are among the weakest and most elusive supramolecular forces.[16,32–37] In first approximation, lone pair-π interactions are to anion-π ones as ion-quadrupole forces are to dipole-quadrupole ones. Moreover, differently from anionic species, lone pair-bearing atoms are ubiquitous, which makes it hard for a weak interaction to emerge from the noise of very large CSD[38] datasets, especially when additional forces are in play (this is the case, for instance, of structural data). These and other considerations are presented in ref. 16. Despite objective difficulties, relevance of lone pair-π interaction for a system as polarized as *s*-tetrazine was ascertained. These tend to be of special relevance when no other directional forces are found and are exemplified by crystal structures of L1 and L2 (Figure 2) among further literature cases.[16]

The microscopic (molecular) aim of this study was to provide a proof of concept, ascribable to a supramolecular interest. The idea is to show that underappreciated forces such as lone pair-π interactions can indeed be engineered and exploited for crystal engineering. The underappreciation of such forces mostly stems from their intrinsic low strength, their low directionality, and the inherent difficulty in designing systems that can effectively take advantage of them, demonstrating their pragmatic use. Still, lone pair-bearing atoms are ubiquitous; hence they need not to be neglected and their possible interactions need to be fully understood.

It is surely possible to conceive an organic anion which bears both an aromatic ring and lone pair-bearing substituents. With an appropriate choice of the charged group it should be possible to have a well-localized charged site with strong tendency to form salt bridges, i.e., a strong preference of the charge-bearing portion of the anion to go for $^{+}$NH ··· anion salt bridges rather than for anion-π contacts with *s*-tetrazine. At the same time, an appropriate choice of the aromatic portion of the anion can disable its competition for the *s*-tetrazine binding site as π-π stacking is much more intense among an electron-rich/electron-poor pair of aromatics, rather than with aromatics with matching electronic features. At that point, having tuned down potential competing interactions, provided lone pair-bearing atoms exists in the anion, lone pair-π contacts should emerge as a relevant interaction involving the substrate and the *s*-tetrazine core.

According to the above, starting from benzene as paragon aromatic, we selected phenol/phenolate, as anionic site with strong H-bond acceptor features, and nitro groups, in the double role of electron-withdrawing groups (tuning electrostatic surface potential [ESP] of the ring) and lone pair-bearing substituents.

In other words, picric acid was selected as the ideal candidate (see on the choice of picrate section) to demonstrate that full control over groups in contact with the *s*-tetrazine ring can be exerted exploiting the stereoelectronic properties of the substrate.

With such a choice of substrate, the reader will quickly notice that this study also has a clear macroscopic (bulk material) interest that could not be concealed.

Picric acid is a well-known explosive, closely related to 2,4,6-trinitrotoluene (TNT). Ammonium picrate, not far from the solid phases that can be obtained by reacting L1-L4 with picric acid, has met military uses. We

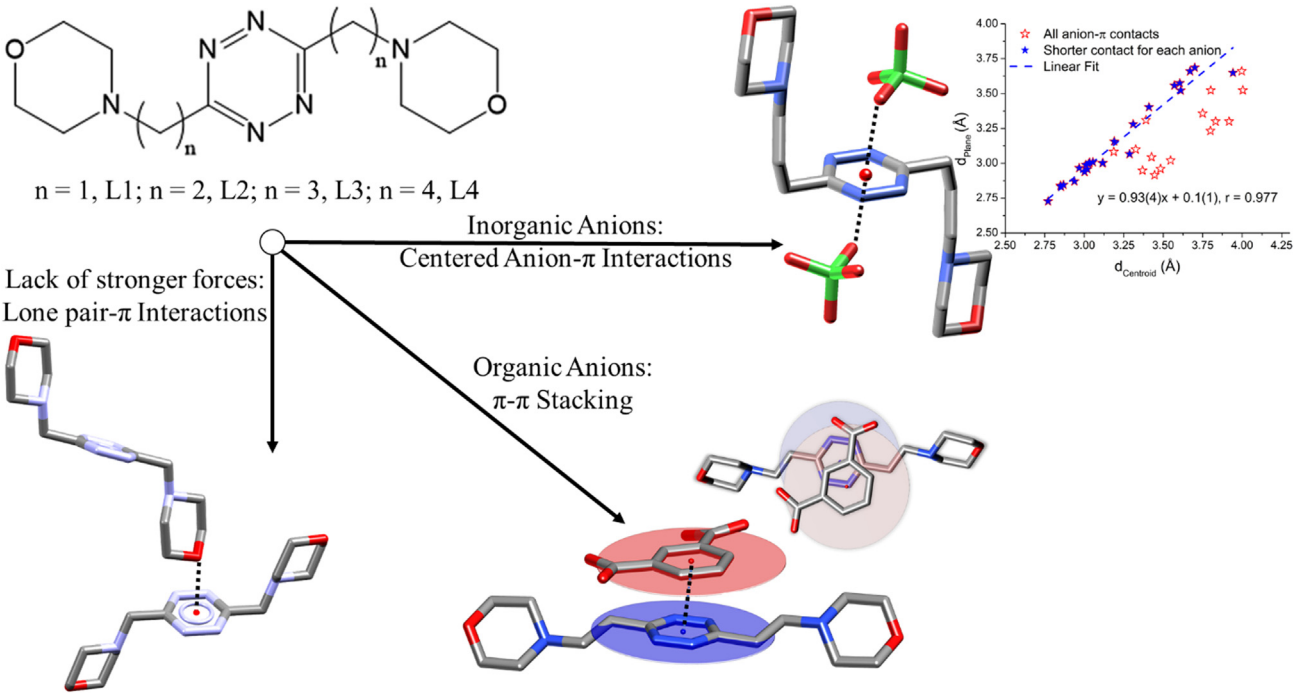

Figure 2. Summary of literature evidence for the L1-L4 series of homologous ligands

Strong and centered anion-π contacts are invariably observed with inorganic anions. Organic anions present the additional π-π stacking interaction mode. In the absence of further, stronger and/or more directional interactions, lone pair-π contacts are encountered instead.

also remind here, again, that explosive character of *s*-tetrazine was among its first applicative interests. Although done with a supramolecular intent, the pairing of picrate with *s*-tetrazine-based receptors clearly puts this study in a high-energy materials context.

As emerging feature, one last interesting point can be envisaged in our study, i.e., crystal engineering of explosives. Full structural elucidation and supramolecular understanding of solid high-energy compounds is not frequently reported together with experimental thermal properties and calculated explosion parameters. Some studies related nature of the interaction on cleavage crystallographic planes (e.g., hydrogen bonds) with shock and friction sensitivity of explosives, relating macroscopic properties to the molecular level.[39–42] Thermostability is equally important to improve the safety of high explosives[43]: this aspect is of particular relevance to the present study, where a clear relationship between picrate intermolecular contacts and thermokinetic parameters is found. In this sense, evidence herein gathered might help the crystal engineering of high-energy compounds aimed at improving their safety of use and storage. Remediating the so-called high energy/high safety contradiction of detonating compounds is a highly coveted goal. While we are generally aware that all manners of devices nowadays rely on technologically critical elements, we seldom remember that the prime usage of explosives remains the one related to the mining industry, which ultimately subtends to our electronics and handheld high-tech commodities.

RESULTS AND DISCUSSION

On the choice of picrate

The electronic structure of picrate, picric acid, and benzene have been determined and compared to achieve information on the electronic reorganization on these molecules. Figure 3 shows that the presence of nitro groups perturbs the electrostatic potential of both picrate and picric acid with respect to that of benzene. In particular, the differences between picric acid and benzene are more marked than those between picrate and benzene; the electrostatic potential of picric acid indeed inverts on the ring moiety with respect to benzene. This is a key feature to avoid π-π contacts among picrate/picric acid and the *s*-tetrazine moiety, which are inhibited by their positive ESP.

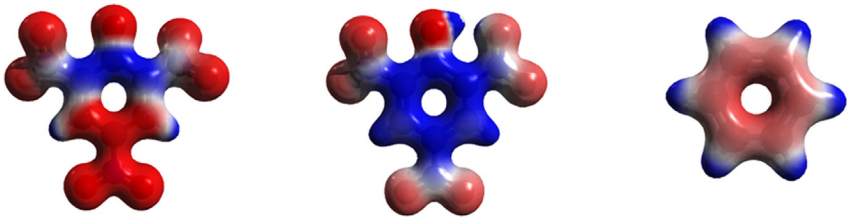

Figure 3. Electrostatic potential of picrate (left), picric acid (center), and benzene (right)

The basic phenolate site remains as the only well-localized charged site with strong tendency to form salt bridges, i.e., to interact with the morpholinium sites of our ligands, thus leaving only the lone pair-bearing nitro groups free to interact with the electropositive *s*-tetrazine moiety. It is important to note that the electrostatic potential of picrate is perturbed by the hydrogen bond when this molecule interacts with ligands. However, Figure 4 shows that, while increasing the hydrogen bond strength, a reorganization of the electrostatic potential does occur; the anion maintains a distribution closer to that of picrate than to picric acid.

Since this will be insightful for the elucidation of obtained crystalline phases, to obtain insights on the orientation of the ortho -NO_2 group of picrate, the rotational barrier has been computed by performing a potential surface scan. The results are shown in Figure 5, where it can be appreciated that the potential barrier height at M06-2x/cc-pVTZ level of theory is within 9 kJ/mol, confirming that the rotation of the nitro group can be affected by the environment. However, CSD data (picric acid and picrate anion, non-metal bound, 1,551 molecules from 1,182 structures), effectively show how such barrier is high enough for the molecule to generally avoid assuming the 60°–120° torsion angle in crystal structures.

Complexes formation in solution

In the case of L2 and L4 it was possible to determine formation constants of 1:1 L:Picr complexes in aqueous solution (other systems present solubility issues as detailed in the experimental section). Results are reported in Table 1.

These complexation phenomena have been studied in detail using the L1-L4 homologous series of ligands and many different inorganic and organic anions.[25,26,28–30] Some general behaviors were found. First, these association equilibria are almost athermic and entropy driven, i.e., they are mostly promoted by desolvation of the *s*-tetrazine and of the portion of the anion in contact with it. Accordingly, salt bridges brought about by ligand protonation offer a marginal contribution to complex stability, while the *s*-tetrazine core remains as a binding site even when the ligands are not protonated. Stabilization offered by salt bridges and charge-charge interactions is generally more significant for smaller, more gathered, ligands, while it becomes less and less significant by increasing the length of the alkyl spacer, although modulation of these effects is also dependent on anion geometry.

The behavior observed for L2 and L4 is fully congruent with this consolidated picture.

Crystal structures description

Overview of shared features

The picrate salts of the L1-L4 diprotonated ligands, indicated with **1**, **2**, **3**, and **4**, respectively, have very different crystal packings, as can be deduced by the variability of crystal systems and crystal cells listed in Table S1. Nevertheless, all the compounds are based on few typical interactions which are found almost unchanged when looking at each single compound.

As shown in Figure 6, L1, L3, and L4 assume very similar conformations, while L2 adopts a quite different and more planar arrangement. However, in each structure, the morpholine N-H^+ hydrogens are divergent, pointing toward opposite side of the ligand molecule, and give charge-assisted $NH^+ \cdots O^-$ H-bonds with picrate anions. Along the L1-L4 homologous series, we notice an even/odd trend: the *s*-tetrazine sits on a center of inversion for L1 and L3 (i.e., **1** and **3** asymmetric units contain only 1 picrate and half ligand), while it does not for L2 and L4 (i.e., **2** and **4** asymmetric unit contains the ligand and two picrate anions). We notice incidentally that a similar odd/even behavior is observed also in $H_2Lx(Picr)_2$ water solubilities (cf. experimental section). Three types of characteristic interactions are found in all structures: 1)

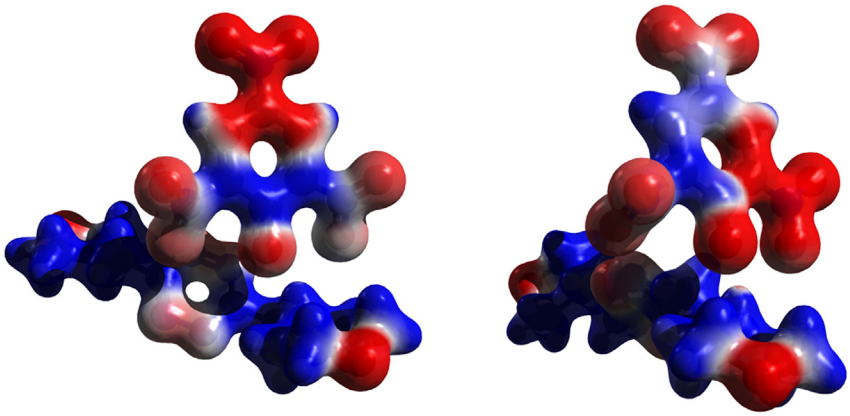

Figure 4. Electrostatic potential of picrate interacting through hydrogen bond with L1 and L2

$NH^+ \cdots O^-$ salt bridges; 2) picrate-picrate interaction (π-π stacking, CH ··· O, and NO ··· NO dipolar interactions); 3) *s*-tetrazine-O_2N lone pair-π contacts.

Salt bridges appear to be the prime interaction in these crystals. As shown in Table 2, in all structures these contacts are quite short and linear, denoting an important contribution of H-bonding to the stabilization of overall packings in **1**–**4**.

The second most representative interaction is picrate-picrate contacts (π-π stacking, NO ··· HC contacts and dipolar interactions among NO_2 groups). Supramolecular organization of picrate anions can vary forming various infinite stacked columns and helices. As packing motifs might be of interest for crystal engineering of explosives, these are described in a following section. Conversely, what is relevant in terms of supramolecular interactions is that the choice of picrate, with its positive ESP, steered the system away from anion-cation π-π stacking. This, together with the strong engagement of the phenolate anionic site in salt bridges, allowed for the emergence of a third type of interaction.

Lone pair-π contacts among nitro oxygens and *s*-tetrazine were found in all crystal structures. This was the supramolecular aim of this study. These interactions are strongly related to the ESP of interacting partners and are elucidated in detail in the following section.

Lone pair-π interactions

Single-point interaction hotspot of s-tetrazine with electron-rich species is above the ring centroid: in this position, the anion can get closer to the ring, maximizing van der Waals contacts, Coulombic attraction, and inductive contribution due to anion-induced ring polarization.[44] This has been demonstrated in silico[44] and is mirrored by experimental distribution of negative charge and lone pair-bearing atoms, subject to anion and lone pair-π interactions, respectively.[16]

However, it should be noted that the intrinsic most positive portion of *s*-tetrazine corresponds to the carbon atoms and coincides with *s*-tetrazine's C-C axis.[15] Accordingly, polyatomic anions might prefer establishing multiple contacts along that axis; this might be even truer for lone pair-π interactions, in view of the fact that any contribution due to induced ring polarization will be reduced with respect to the anion-π case. In those scenarios, anion/lone pair-bearing atoms are expected to be found aligned to the C-C axis, if possible.[16] This behavior is perhaps accentuated in the case of our complexes due to the O ··· O bite of nitro groups being comparable to the C ··· C distance in *s*-tetrazine.

In the case of our ligands, the smallest L1 features the morpholinium H-bond donor and the *s*-tetrazine moiety very close to one another, fostering cooperativity among binding forces (Figure 7).

Beyond the N1-O2 salt bridge, the phenolate O2 oxygen engages in a short contact with *s*-tetrazine C6 carbon (3.110(2) Å) with an angle compatible with lone pair localization (C7-O2-C6 angle 122.9(1)). What is most interesting is the O5-C6′ lone pair-π contact, which is even shorter (2.891(2) Å). It should be noted

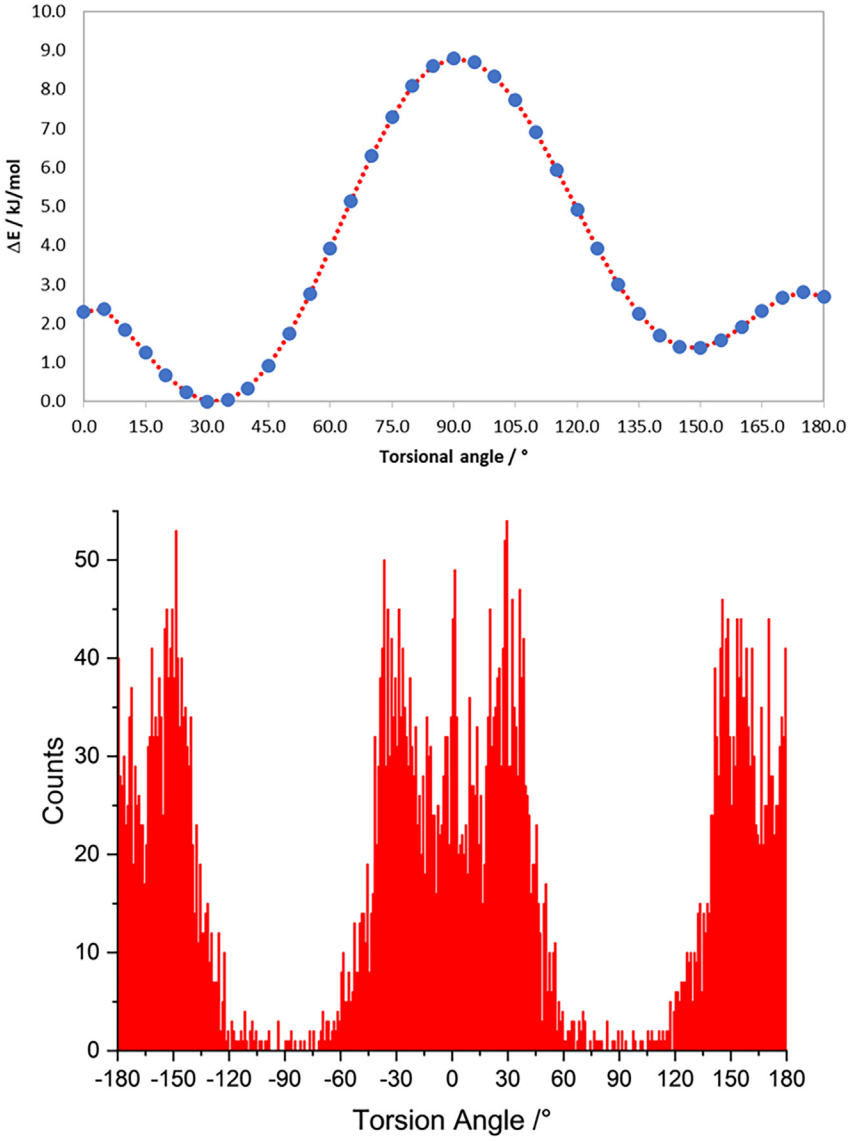

Figure 5. Top: Torsional angle for the -NO_2 group in picrate at M06-2X/cc-pVTZ level of theory; bottom: experimental distribution of torsion angles in the CSD (angle bins of 1°)

that, given the small molecular size of the ligand, establishment of this contact requires significant rotation of the nitro group, which deviates from benzene ring plane for more than 40° (Table 3). Despite that, the N5-O5-C6′ does not manage to properly align at 120°, as in the ideal geometry for sp^2 oxygen (although the larger angle ensures shorter NO ··· C contact).

When a Hirshfeld surface approach is employed, a lone pair-π interaction contact area can be individuated (Figure 8). Moreover, as for all directional interactions, a sharp tip pertaining to O-C contacts can be found in the fingerprint plot of the adduct, signaling that in this case NO dipole-*s*-tetrazine ring quadrupole interaction has a certain intensity and a markedly directional character.

Although the rotation barrier for NO_2 groups was not found to be exceptionally high, about 9 kJ mol^{-1} (cf. on the choice of picrate section), this range of energies is compatible with what can be expected for lone pair-π interactions. Free energy changes ($-\Delta G^0$) for the coordination of mono- or divalent inorganic anions to neutral, not-protonated, L1-L4 ligands in solution, range between 10 and 17.5 kJ/mol,[25,26] in good agreement with previously determined free energy changes for polarized pyrimidine ligands

Table 1. Formation constants of picrate complexes with L2 and L4 ligands determined in aqueous NMe_4Cl 0.1 M at 298.1 ± 0.1 K

	log *K*	
Equilibrium	L2	L4
$L + Picr^- = [LPicr]$-	3.39 (9)	3.09 (5)
$HL^+ + Picr^- = [HLPicr]$	3.47 (9)	3.36 (4)
$H_2L^+ + Picr^- = [HLPicr]^+$	3.61 (9)	3.36 (8)

Figures in parentheses are standard deviations on the last significant figures.

($-\Delta G^0$ = 8.6–12 kJ/mol).[45] These values are comparable to those observed for L2 and L4 in solution studies. While it is not immediate to transfer solution data (which includes solvation free energies) to the solid state, it is manifest that NO dipole-*s*-tetrazine quadrupole interaction, together with further supramolecular interactions such as NO ··· HC contacts, is strong enough to compensate for the energy cost of rotation about the C-N bond of the nitro groups. In other words, these interactions affect both crystal packing and conformation of the picrate anion, strengthening the idea that it is possible to intervene on the stereoelectronic properties of an explosive molecule through crystal engineering.

Next, we need to demonstrate that this is not the sole instance among L1-L4 crystal structure, nor that this is casually brought up by the global arrangement of the interacting groups on both partners. In this sense, the L1-L4 series is highly instrumental as increasing the length of the spacer renders morpholinium and *s*-tetrazine sites progressively unable to show cooperativity in substrate binding. It was previously demonstrated that this did not shut down anion-π binding abilities of the ligands in the slightest.[25,26]

L2 situation is even more revealing (Figure 9). A single lone pair-π short contact is found: O5-C8 2.975(5) Å. Despite that, L2 desperately tries to bring O4 in contact with C7, i.e., aligning O4 and O5 nitro oxygens to the C7-C8 axis. A compromise is achieved where C15-C16-N7-O5 torsion angle reaches the surprisingly high value of 78.3(4)° (cf. Figure 5) and the O4-C7 contact remains quite long 3.266(5). This somewhat testifies the electrostatic nature of the interaction, and its ability to be sensed through space, although within very short distances. According to the longer contact with respect to L1, the C-O contact peak in the fingerprint plot is less sharp, although the lone pair-π contact can still be observed in the Hirshfeld surface of H_2L2^{2+}. We notice, incidentally, that the shape of the fingerprint plot area associated with lone pair-π contacts is the same one which we demonstrated typical of anion-π contacts[46]: this is because the topology of the interaction is similar. The other face of the *s*-tetrazine is also telling. Two different anions approach it, with none of them, due to their compresence, being able to solely interact with the s-tetrazine. The best agreement, satisfying all instances, is that C7 and C8 engage in long-range electrostatic interactions with O12 and O9. Contacts remain slightly longer than the sum of the van der Waals radii (O12-C7

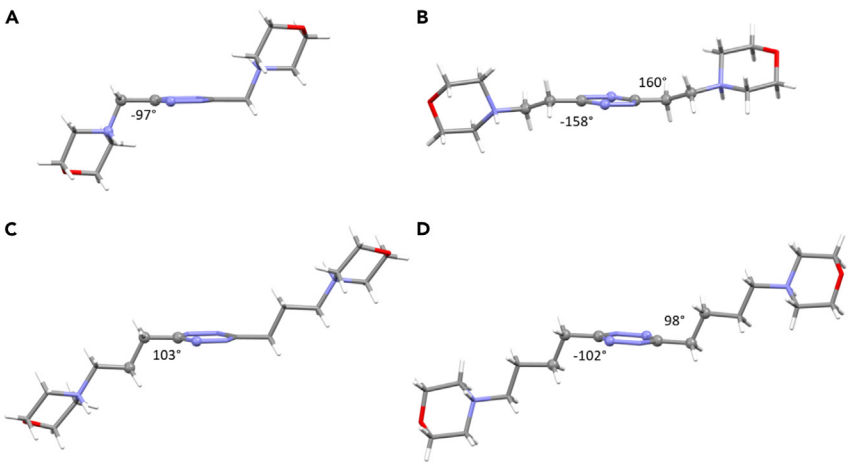

Figure 6. Overview of ligands' conformation
Ligands' conformations in the $H_2L(picrate)_2$ salts (L1 – 1 (A), L2 – 2 (B), L3 – 3 (C), L4 – 4 (D)).

Table 2. Details for the charge assisted $NH^+ \cdots O^-$ H-bonds between H_2L^{2+} cations and picrate anions in compounds 1–4

$NH^+ \cdots O^-$ Salt Bridge	1	2	3	4
H ··· O (Å)	1.85(2)	1.71(4)/1.69(4)	1.84(2)	1.75(2)/1.82(2)
N ··· O (Å)	2.675(2)	2.633(4)/2.624(4)	2.737(2)	2.647(1)/2.679(1)
N-H-O angle (°)	152(2)	159(4)/158(4)	156(2)	162.74(1)/165.83(1)

Values in parentheses are associated standard deviations.

3.118(5) Å, O9-C8 3.403(5) Å), signifying very weak interaction; yet, the N-*O*-C angle is found much closer to ideal sp^2 geometry (N10O12C7 117.7(2)°, N9O9C8 117.5(2)°, i.e., the O lone pair points right toward the C atom), and no significant perturbation of picrate planarity (torsion around C-N bond is 8.3(5)° and 15.1(5)° for O9 and O12 containing molecules) is found. In other words, lone pair-π interaction might be significant and intense at short distances, when packing allows, yet it can also be a loose dipole-quadrupole interaction whenever other more intense and directional forces orchestrate the packing. The point is that such an elusive force is manifest in all instances of L1-L4 complexes with picrate.

Similar considerations can be drawn for L3 (single centered interaction, Figure S1) and L4 (NO_2 perfectly aligned with C-C axis without the need of significant distortion, Figure S2).

An overview of each crystal structure is presented in the supplemental information (SI), while global metrics are gathered in Table 3.

Picrate-picrate interactions: Slip planes, crystal density, and extent of contacts

As stated, picrate-picrate interactions are a major feature in crystal packing in compounds **1**–**4**.

In the salts of L2 (**2**) and L4 (**4**), pairs of π stacked anions are clearly recognized which are in contact with other close couples through their -NO_2 groups (O ··· O distances in the range 2.8–3.3 Å – Table S2).

Such important and apparently counterintuitive O ··· O short contacts are commonplace in these series of structure and deserve immediate comment. They arise from dipolar interactions among nitro groups: a clarifying example is presented in Figure 10 (form crystal structure **4**), where it can be seen that in trying to establish mutual N10 ··· O8 (2.985(1) Å) and O11/O12 ··· N9 (3.241(1) and 3.218(1) Å, respectively) mutual

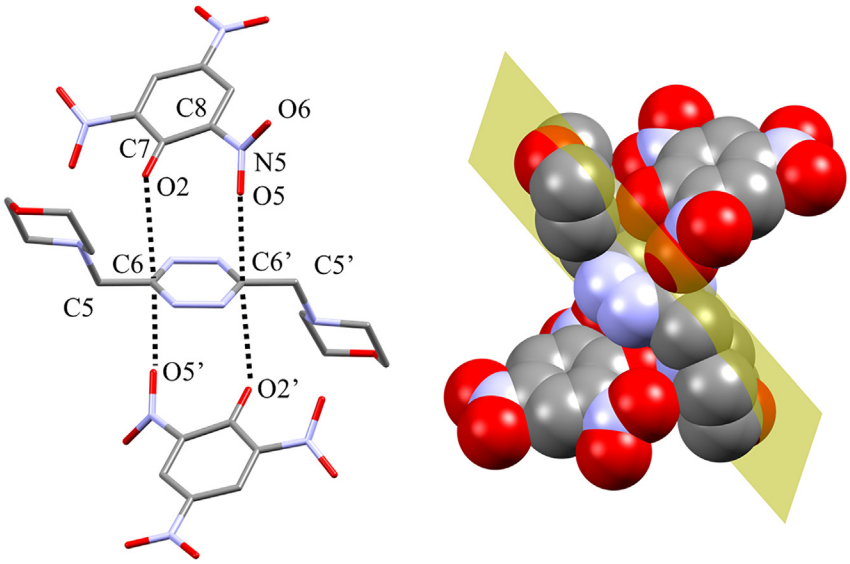

Figure 7. Anion-π contacts found in compound 1

Space filling model shows the torsion of the ortho NO_2 group to align along the *s*-tetrazine C-C axis plane (passing through C5, C6, C6′ and C5′, yellow).

Table 3. Detail of lone pair-π contacts in compounds 1–4 (shortest contact for each crystal structure)

Ligand	N-O ··· C Angle (deg)		C-NO2 Torsion (deg)		NO ··· C Distance (Å)		d_{plane} (Å)	d_{offset}[a] (Å)	$d_{centroid}$ (Å)
L1	N5-O5 ··· C6	145.0(1)	C7C8N5O5	−42.3(2)	O5 ··· C6	2.891(2)	2.886	1.151	3.107
L2	N7-O5 ··· C8	111.6(3)	C15C16N7O5	78.3(4)	O5 ··· C8	2.975(5)	2.893	1.876	3.448
L3	N6-O8 ··· center	118.58	C9C14N6O8	−126.6(2)	O8 ··· center	2.915	2.897	0.323	2.915
L4	N8-O6 ··· C9	99.51(9)	C20C19N8O6	−7.7(2)	O6 ··· C9	2.936(2)	2.889	1.751	3.378

[a]To provide proper context: an offset of 0 Å corresponds to perfectly centered anion-π interaction; C and N atoms in s-tetrazine are 1.28 and 1.38 Å apart from the ring centroid, respectively.

NO ··· NO interactions, O ··· O contacts are also unavoidable and they result in the shortest contacts (O11 ··· O8 2.828(2) Å, O12 ··· O8 3.212(2) Å, and O12 ··· O9 3.047(1) Å, respectively). This concept will be further expanded at the end of this section.

The discussion of crystal packing features is undertaken from the most likely slip planes point of view.

Slip planes are among the most important packing features for energetic materials.[39,41,42,47] The ability of closed packed planes—necessary to ensure high material and hence energy density—to slip effortlessly upon each other (either individually, in an interfacial shear mode, or collectively, in a bulk-shear mode, i.e., like a deck of cards), provides a way to safely dissipate the energy provided by external mechanical stimuli.[41,42] In other words, scarcely interpenetrated slip planes whose molecular boundaries do not share strong intermolecular interactions (e.g., H-bonds, which might be the cause of intense molecular friction upon plane slipping), should provide a way to remediate the high energy/high safety contradiction of energy materials by decreasing their shock sensitivity.

Accordingly, in line with the supramolecular attention of present study, we evaluated most likely slip planes in all crystal structures using CCDC Mercury[48] routine and checked supramolecular interactions among and around them.

We report here full details for the L1 complex and an overview of packing/slip planes features of the whole series. Further details can be found in the supplemental information.

In **1**, the most likely slip plane develops along the (020) direction (Figure 11, Table 4). This plane separates closed-packed slabs constituted by salt-bridged ligands and couples of π-stacked anions

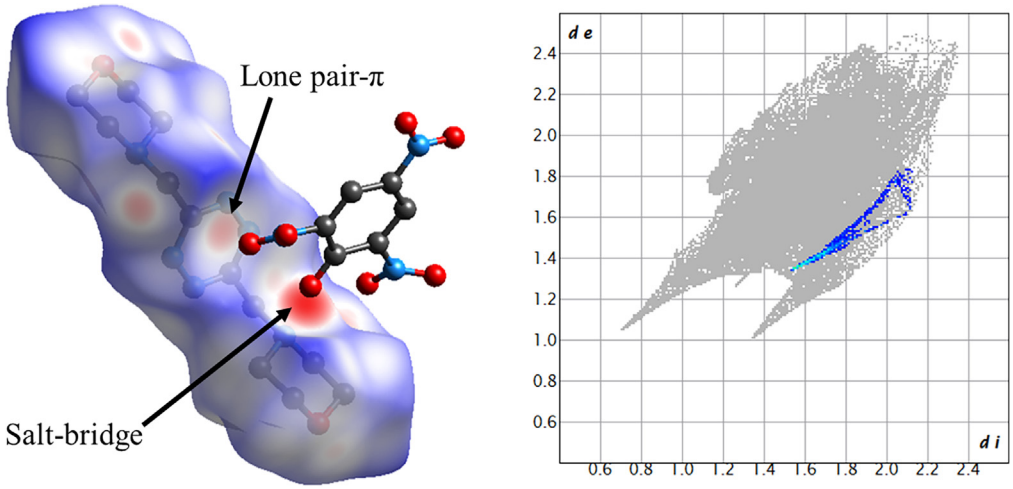

Figure 8. Hirshfeld surface of H_2L1^{2+} in compound 1, denoting salt bridge as well as lone pair-π interactions
Fingerprint plot of H_2L1^{2+} (gray) shows marked O ··· C contacts (blue-to-red CrystalExplorer standard scale) originating a marked tip-like feature pertaining to NO ··· $C_{tetrazine}$ interactions.

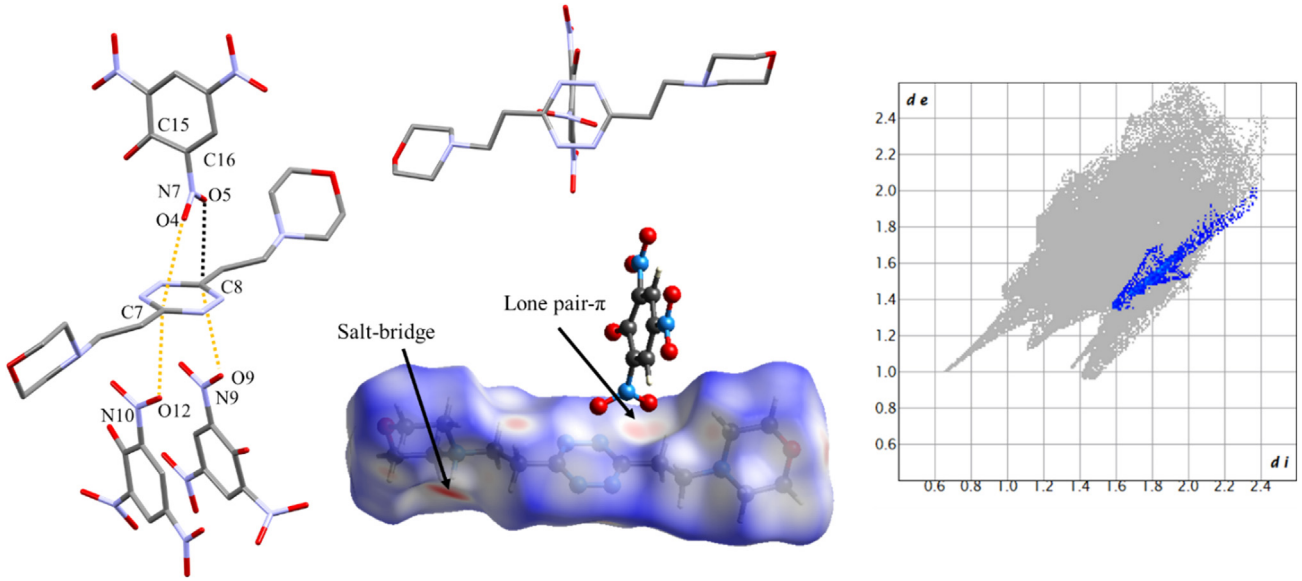

Figure 9. Overview of lone pair-π interactions in compound 2

Left-to-right: overall arrangement and short contacts, twisting of NO_2 groups, Hirshfeld surface of H_2L2^{2+} showing both salt bridge and lone pair-π interaction hotspots and fingerprint plot of H_2L2^{2+} with O ··· C interactions highlighted.

(Figure 11A and 11B). The only O ··· O (nitro-nitro) short contacts below the van der Waals distance also develop within the two slabs parallel to the slip plane (i.e., along the stacking direction of the picrate anions).

As a matter of fact, the slip plane presents no hydrogen bonds, nor the protruding nitro groups are in contact among them (O ··· O contacts through the slip planes are all > Σvdw radii +0.4 Å), while it separates densely packed slabs with strong intermolecular cohesive forces (salt bridges and π-π stacking). This would be a highly desirable property to obtain a low shock-sensitive material.

For what topology is concerned, the found slip plane is moderately corrugated (rugosity: 1.293, Table 4), with the interpenetration of the slabs being less than 1 Å (−0.976 Å, expressed as distance among interpenetrated slabs, Table 4). An overview of topological feature of the slip plane molecular surface (as sensed by a 1.2 Å probe, drawn with 0.1 Å grid spacing) show how grooves appear to be relatively well aligned for sliding, at least along the c direction.

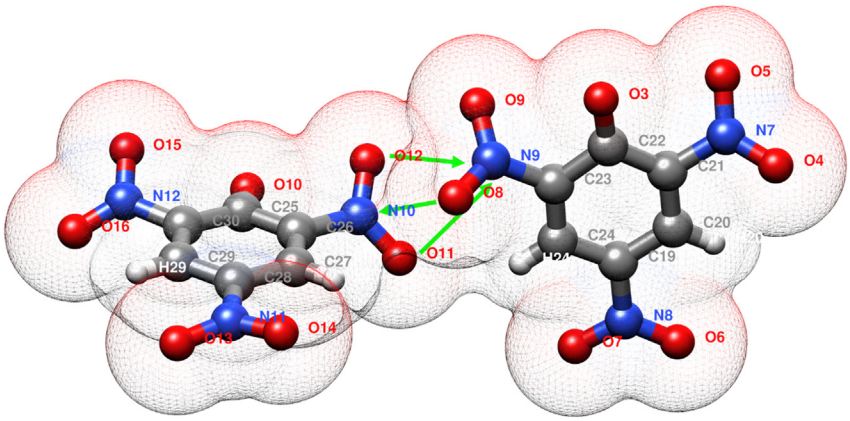

Figure 10. Exemplificative detail of picrate-picrate contacts (from 4)

In trying to establish expected nitro-nitro dipolar interactions (green arrows) short oxygen ··· oxygen contacts (hinted by mesh representation of van der Waals surface) are unavoidable due to picrate geometry.

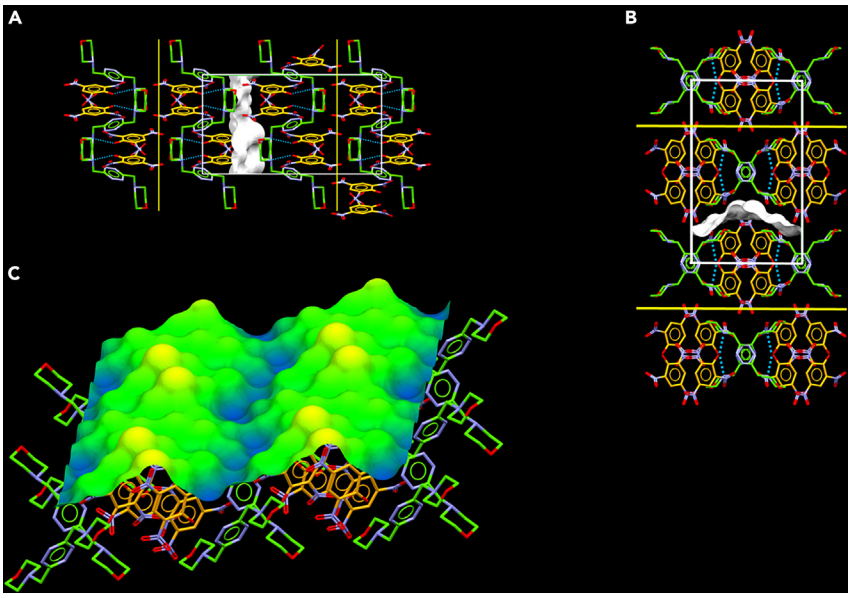

Figure 11. View of the (020) slip plane found in compound 1

(A) View along the *a* crystallographic direction showing the slip plane (white molecular surface, repeats as yellow planes) and the two close packed slabs adjacent to it, featuring ligand-anion salt bridges (cyan) and zigzag chains of π-stacked anions (orange).

(B) View along the *c* crystallographic direction showing the slip plane (white molecular surface, repeats as yellow planes) and the two close packed slabs adjacent to it; salt bridge pattern (cyan) is highlighted.

(C) 2 × 2 unit cells depiction of the slip plane molecular surface colored according to its topology using a blue-to-yellow palette to show depths-to-heights difference (slab separation −0.976 Å, Table 4).

No further reasonable slip planes were found for **1**, the second most likely slip plane, developing in the (1-1-2) direction, and the third one, along (11-2), feature a much higher slab interpenetration (both 2.096 Å, Table 4).

In **2**, the situation is quite similar (Figure S3).

Slip plane develops in the (002) direction, separating slabs of salt bridge-paired anions and ligands, with picrate anions arranged in stacks. The similarity is particularly evident if views of slip planes of **1** in the *a* direction (Figure 11A) and *b* view of slip plane in **2** (Figure S3b) are confronted.

Table 4. Overview of potential slip planes in the 1–4 crystal structure series

Slip Plane Features	1	2	3	4
Orientation	(020)	(002)	(101)	(40-2)
Offset (Å)[a]	−5.162	0	−2.996	0
Slab Separation (Å)[b]	−0.976	−1.177	−2.674	−2.281
Repeat Distance (Å)	10.324	10.554	5.992	4.779
Hydrogen Bonds	No	No	No	Yes
Hydrogen Bond Dimensionality	–	–	–	0D, discrete
Rugosity[c]	1.293	1.287	1.580	1.396
Perpendicular Slip Plane[d]	No	No	No	No
Second Smallest Slab separation (Å)[e]	−2.096	−2.623	−2.770 (1–12) and (112) planes	−3.283

[a]Offset in the normal direction with respect to the plane family specified as "Orientation".

[b]Distance of adjacent slabs through the slip planes (negative values indicate layer interpenetration).

[c]As ratio of "real" (1.2 Å probe, 0.1 Å grid spacing) surface area to projected "geometrical" area.

[d]Presence of second perpendicular slip plane is of potential high interest for mechanical stress dissipation.

[e]Second smallest interpenetration among further slip planes candidates (the highest the interpenetration, the more the energy required for slipping).

Although complicated by the compresence of two non-equivalent anions, *a* view (Figure S3a) shows picrate π-stacked columns developing in the two slabs separated by the slip plane.

Again, none of the relevant and directional interactions keeping together the dense slabs (salt bridges and π-π stacking) needs to be broken to allow slipping along the selected plane. No O ··· O contacts below the van der Waals contact distance are found, with those formed through the slip plane been quite long (>Σvdw radii +0.2 Å).

For what topology is concerned, although the global rugosity is comparable to the **1** case, we observe a less trivial arrangement of grooves and ridges, probably offering more hindrance to slipping.

For crystals of **3** and **4** the analysis is presented, although the found planes clearly show that these crystals are much more rigid and less prone to sliding.

For **3**, the maximum slab distance is −2.674 Å, i.e., slabs are interpenetrated more than twice as much with respect to **1** and **2** cases. Still, the crystal packing can be discussed from this plane point of view. The found plane belongs to the (101) family. The *a* view (Figure S4a) is particularly descriptive, as it shows π-stacked columns of picrate anions completely paneled by a diamond of salt-bridged ligands. Although salt bridges run parallel to the plane, slipping requires breaking of π-π stacking contacts of picrate anions in one direction and breaking of picrate-*s*-tetrazine lone pair-π interactions in the other (Figure S4); it should be noted that π-stacks of anions here are not freely displaceable due to the ligand diamonds surrounding them. Beyond the breaking of stabilizing interactions upon slipping (a feature not observed for **1** and **2**), the significant slab interpenetration (2.674 Å, Table 4) also draws a complicated herringbone elevation motif at the proposed slip surface. A second set of two planes, featuring a similar slab separation with respect to the one considered (both −2.770 vs. −2.67 Å, Table 4), were tentatively considered, although they do not appear more promising than the evaluated one (a quick view of their unfavorable topology is shown in Figure S5).

Packing of **4** has strong similarities with the one of **3**, with ligand-defined diamonds hosting not a single stack of picrate anions (cf. Figure S4a) but repeats of π-stacked pairs of anions piled upon each other (cf. Figure S6b).

Topology would be somewhat better than in the case of **3** due to overall reduced rugosity and to a softer repeat of grooves and crests, with a less complicated surface motif. Still, slip plane in **4** appears as the least promising in terms of mechanical shock dissipation as salt bridges cross it. This means that the single most intense intermolecular interaction type in the crystal structure must be broken to allow slipping on this plane. No better slip plane alternatives were found (second shortest slab separation −3.283 Å, Table 4).

In brief, L1 and L2 complexes appear to possess desirable features in terms of alternating high-density planes, necessary for high energy density, and low-density slip planes, which could help reducing shock sensitivity. L3 and L4 instead feature a more homogeneous density in the three dimensions, with least close-packed planes not spaced enough to allow a slipping behavior. It is also worth mentioning that the shorter L1 and L2 ligands result in the similar **1**/**2** packings; the same is true for the longer L3 and L4, originating similar **3**/**4** packing features. The origin of such different arrangements is probably to be found in the match/mismatch of ligand/anion mutual size.

In terms of nature of forces in play, the analysis of the crystal packings of these four picrate salts evidences the homogeneity of the intermolecular interactions established. The main difference, again, appears to be the number of methylenic groups in the linkers connecting the tetrazine and the morpholine moieties. It changes from **1** (L1) to **4** (L4), while the cation:anion stoichiometry ratio is constantly equal to 1:2. This means that the crystal density also varies continuously, and it assumes the minimum value of 1.509 g/cm^3 in compound **4** (L4) and the maximum value of 1.601 g/cm^3 in compound **1** (L1)

An interesting point in terms of material properties (cf. thermal analysis section) concerns the extent of picrate-picrate contacts. In particular, it would be of interest to quantify them and estimate whether the different architectures found in compounds **1**–**4** result in increased or decreased picrate-picrate connectivity.

Table 5. Computed picrate-picrate extent of contact quantities together with experimental DSC-determined kinetic parameters (see dedicated section below)

Sample	C ··· C contacts (%)	O ··· O contacts (%)	Contact Extent (%)	Hirshfeld Surface (Å^2)	Contact Extent (Å^2)	E_a (kJ/mol)	A (min^{-1})	R^{2c}
1	2.8	7.9	10.7	209.7	22.4	517	$1.8 \cdot 10^{52}$	0.9936[d]
2[a]	4.3	9.1	13.9[b]	206.77	28.7[b]	336	$4.80 \cdot 10^{32}$	0.9957
	4.3	10.1		206.34				
3	8.3	7.8	16.1	207.84	33.5	164	$1.60 \cdot 10^{13}$	0.988
4[a]	4.1	12.1	16.0[b]	208.54	33.3[b]	153	$1.40 \cdot 10^{12}$	0.9932
	4.1	11.7		208.15				

[a]Two non-equivalent picrate anions present in the crystal.
[b]Average mediated on the two different anions.
[c]Correlation coefficients of the linear fitting of the plots $\ln\frac{\beta}{T_p^2}$ vs. $\frac{1}{T_p}$ for the obtainment of E_a and A according to the Kissinger model.
[d]In this case the plot was obtained by using the data acquired at three lower heating rate (5, 10 and 20°C/min) because the thermal process at high heating rate (50°C/min) was so intense that no shift in the temperature of the peak was detected with respect to the curve registered at 20°C/min.

To answer this question, we started from two simple observations.

First, the molecular surface of picrate is mainly composed of O and C.

Since we showed that picrate-picrate interaction is mainly of π-π stacking and dipolar type, and that there are essentially no C ··· C or O ··· O contacts among Lx and picrate anions (most ligand-anion interactions are CH ··· O, O ··· C/N, i.e., lone pair-π contacts, or NH ··· O, i.e., salt bridge), we can use the extent of C ··· C and O ··· O contacts to estimate the extent of picrate-picrate contacts in our crystal structures. These quantities are not biased due to ligand-picrate interactions (CH ··· O, C/N ··· O, NH ··· O, as said) and are expected to be present as major components among picrate anions in contact with each other (*a priori*, because their Hirshfeld surface, as their van der Waals one, will be primarily made of O and C, as said, as well as *a posteriori*, because indeed O ··· O and C ··· C contacts are often observed as the most significant ones, cf. earlier discussion and Figure 5).

Accordingly, the extent of picrate-picrate contacts is directly proportional to C ··· C and O ··· O contacts, which can be computed simply by calculating Hirshfeld surface for all picrate anions (twice and averaging for crystal structures containing 2 non-equivalent picrate anions) and computing "C ··· C contacts + O ··· O contacts" percentages. These percentage quantities can eventually be re-translated into contact areas expressed in Å^2 (small variability among picrate global Hirshfeld surface area among L1-L4 crystal structures is both expected and found: average 208 ± 2 Å^2, minimum 206.34 Å^2 (**2**), maximum 209.70 Å^2 (**1**)).

According to this procedure, data in Table 5 are obtained, which point out that extent of picrate-picrate contact sensibly increases along the **1**–**4** series of compounds, namely by about 50% in moving from compound **1** to **3** and remains almost constant from **3** to **4**. This information will be instrumental in the following. We notice that this microscopic (molecular) information is not manifest *per se* in the density descriptor, which is a macroscopic (bulk) quantity and only changes by about 6% along the series. While importance of material density for its explosive properties is well known, we will show in the following how molecular contact details can be exploited to expand structure-properties correlations to thermal properties.

Thermal analysis of compounds 1–4

Thermal analysis was used to assess the thermal stability and to calculate the thermokinetics parameters of the compounds. The TGA and DTG profiles of the L1-L4 ligands, together with those of picric acid, for comparison, are shown in the supplemental information (Figure S7). The thermal stability (i.e., the highest temperature at which no weight loss occurs) does not increase proportionally with the length of the spacers groups: instead, it varies in the order L4>L1>L3>L2>PA.

The thermal decomposition process of compounds **1**–**4** takes place through a two-step process. Figure 12 shows the TGA and the DTG profiles acquired at four rates (5, 10, 20°C, and 50°C). It is evident that for **1** the first step is the most "intense", especially at high heating rates, producing a sudden weight loss of about

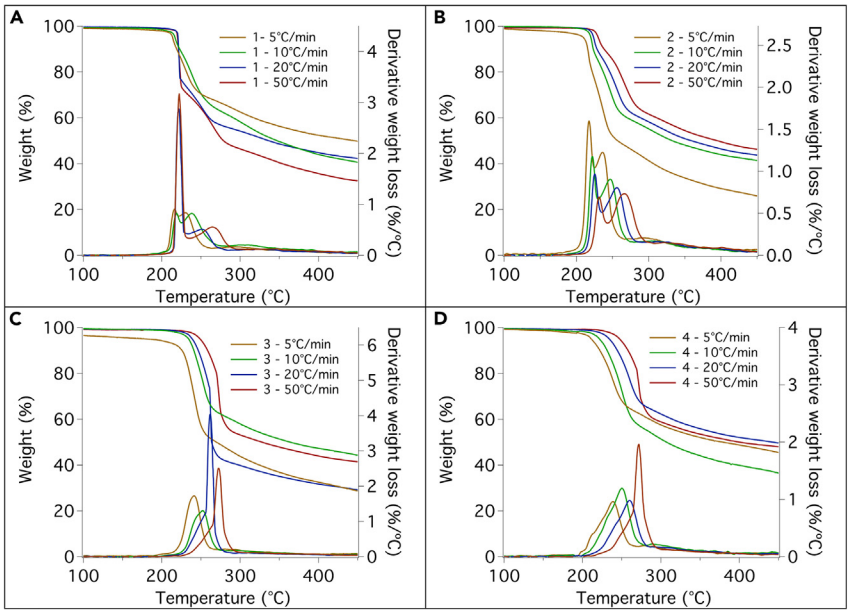

Figure 12. Weight loss profiles of compunds 1–4

Weight loss profiles and correspondent derivative curves registered at four different rates for compounds **1** (A), **2** (B), **3** (C), and **4** (D).

25% (for 20°C and 50°C/min). Increasing the length of the ligand, the situation reverses, and compounds **3** and **4** show an accentuated second step (at high heating rates) while the first step occurs more gradually. No accentuation with the increasing rate is observed for compound **2**.

Acquiring the thermal scans at different heating rates enabled us to investigate the non-isothermal kinetic of decomposition of **1–4**. Kissinger model was used to calculate the kinetic parameters of thermal decomposition of the compounds, i.e., the apparent activation energy (E_a) and the preexponential constant (A), using the first DTG peaks.

Kissinger model can be expressed as follows:

$$\ln\frac{\beta}{T_p^2} = \ln\frac{AR}{E_a} + \left(\frac{1}{T_p}\right)\left(\frac{-E_a}{R}\right)$$

where E_a is the apparent activation energy (kJ/mol), β is the heating rate, R is the gas constant (8.314 J/K mol), A is the preexponential factor (1/min), and T_p is the peak temperature (K).[49,50] From the linear fitting of the $\ln\frac{\beta}{T_p^2}$ vs. $\frac{1}{T_p}$ plot, the activation energy and the preexponential factor can be obtained for each system. These values together with the correlation coefficients of the fittings are reported in Table 5. Data plots are reported in the supplemental information, Figure S8.

The heat flow signal for all the decompositions was acquired simultaneously to the weight loss. The data obtained for the four compounds at 10°C/min are shown in Figure 13 and can be compared to the DSC data obtained for the ligands alone in the same figure (which also shows the picric acid thermogram).

It can be shown that the data in Table 5 show an interesting correlation.

In fact, if experimental activation energies or preexponential factors (in the latter case log values, since variability is extremely large) derived from Kissinger model are plotted versus extent of contact (either expressed as % or in $Å^2$), a linear correlation is found (Figure 14).

It should be noted that the classical Arrhenius-like kinetic model, $k = A\,e^{\left(\frac{-E_a}{RT}\right)}$, where all symbols have the usual meaning, can be rearranged to show that the natural logarithm of the rate constant k,

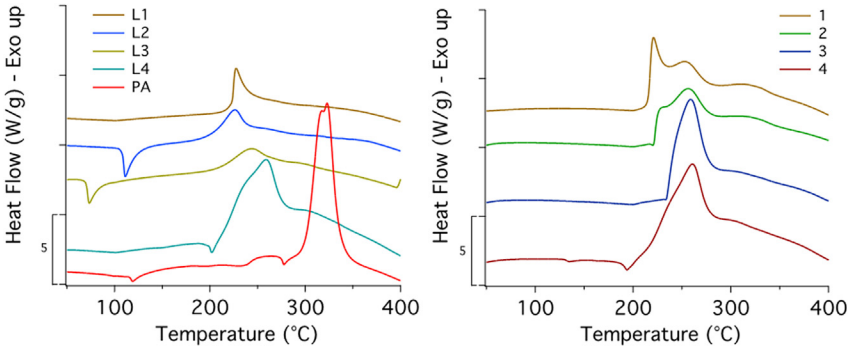

Figure 13. DSC curves of L1-L4 and PA and of compounds 1–4 acquired at 10°C/min
Curves are arbitrary offset for the sake of clarity.

$\ln(k) = \ln(A) - E_a/RT$, depends linearly on both ln A and on $-E_a$. Since we showed that both $\log_{10}(A) = \ln(A)/2.303 \propto$ (-ppc) and $E_a \propto$ (-ppc), where ppc are picrate-picrate contacts, also ln(k) as a whole is a linear function of pcc, which translates into stating that rate constant k depends exponentially on pcc.

This seems to indicate that, for a series of homologous ligands forming crystal structures with the same principal interactions, the thermal sensitivity of the resulting energetic materials, expressed as the rate constant of the thermal decomposition process, is an exponential function of the extent of picrate-picrate contacts in the crystal. Namely, by increasing picrate-picrate contacts one decreases both the activation energy and the preexponential factor, while when picrate anions are more spaced out, a higher activation energy needs to be provided, yet, when that happens, explosive discharge of energy is much faster (higher preexponential factor).

In plain words, our exercise in supramolecular chemistry demonstrates that it is possible to tune the thermal stability of high-energy materials (read *"safety of explosive compounds"*) by crystal engineering.

This appears as a relevant and interesting result that might foster future development.

In silico characterization of explosive properties of compounds 1–4

Explosive properties of compounds 1–5 were calculated with the EXPLO5 software (version 6.06.01)[51] (Table 6).

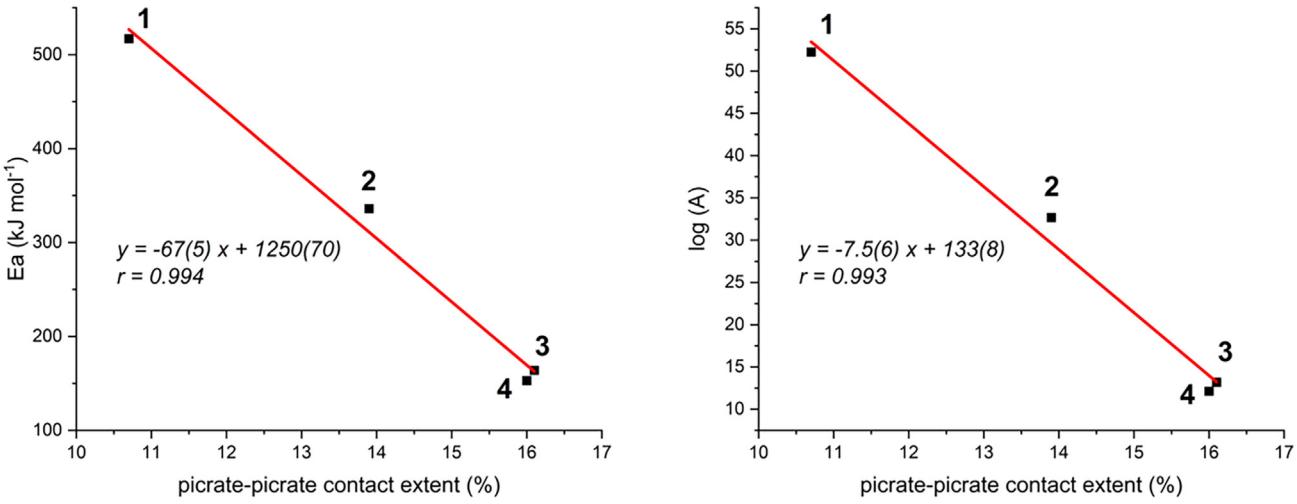

Figure 14. Linear correlation among experimental thermokinetic parameters from DTG and picrate-picrate contact extent

Table 6. EXPLO5-calculated explosion parameters for compounds 1–4 (TNT as reference), including oxygen balance (OB), steady state detonation velocity (D_{CJ}), pressure (P_{CJ}), and temperature (T_{CJ}), heat of detonation (ΔH_d), and Gurney velocity (G)

Compound	OB	D_{CJ} (km/s)	P_{CJ} (GPa)	T_{CJ} (K)	ΔH_d (kJ/mol)	G (km/s)
1	−97.5	6.894	17.3	2975	4.821	2.326
2	−106.4	6.761	16.3	2827	4.700	2.279
3	−114.8	6.556	14.9	2713	4.688	2.180
4	−122.5	6.493	14.3	2600	4.665	2.104
TNT	−74.0	6.941	18.8	3227	4.576	2.368

Discrepancy among calculated and experimental properties are <1% (<3% for G) for the TNT reference compound.

The software employs crystal experimental density, formulas and heats of formation of crystalline compounds. The latter have been calculated via DFT formation enthalpies obtained through a series of isodesmic reactions and estimation of reticular energies as described in the experimental section (cf. Scheme 1 and related discussion). Thermodynamic data obtained for the $H_2L_x^{2+}$ cations (x = 1–4) and of the resulting **1–4** picrate salts are reported in Table S3.

Among the products of detonation at the CJ state, there are significant amounts of H_2O, C, N_2, CO, CO_2, CH_2O_2, minor amounts of NH_3 and CH_4, and trace amounts of other species.

The **1–4** series behaves as expected: compounds are found more explosive in the **4** to **1** order.

This is both in agreement with experimental densities and mirrors the trend of DSC-determined preexponential factors (increasing in the **4** to **1** direction, cf. earlier text). The trend of activation free energies is instead reversed: this means that the most explosive compound, **1**, is also the safest to handle in terms of thermal decomposition activation energy, a fact now explained in view of picrate-picrate contact extent.

For comparison, a common high explosive TNT is also shown in Table 6.

All the examined compounds are slightly inferior to TNT in view of detonation parameters except the detonation heat. This is mostly because of their highly negative oxygen balances and lower densities.

The results obtained for the four examined compounds are all relatively similar to each other, and they all can be considered high explosives.

Closing remarks

Herein we provided a triple proof of concept.

First, one is free to decide which moiety of a substrate, among its anionic site, aromatic surface or lone pair-bearing substituents will interact with the aromatic portion of a receptor (s-tetrazine in our case) in the solid state. This can be done through an appropriate choice of stereoelectronic features. Since this intended to be a demonstrative example, stereoelectronic features of the guest were engineered, in a sort of "reverse crystal engineering". We have no doubts that this can be applied also in the standard direction, i.e., on the design and molecular engineering of a host for a predetermined target guest.

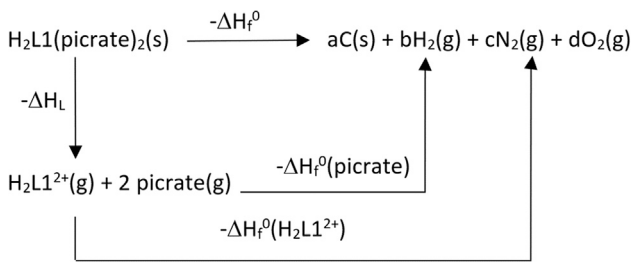

Scheme 1. Born-Haber cycle employed for calculating the heat of formation of the $H_2L1(picrate)_2$ salt

In second instance, under the right conditions, not only lone pair-π interactions manifest themselves, but they are, for all intents and purposes, supramolecular forces we can rely on, in combination with all others, to stabilize supramolecular adducts and orient the three-dimensional organization of solid phases. We underline that the "under the right conditions" clarification does not diminish the relevance of this statement in the slightest: this simple note is true for most instances of nowadays popular interactions (for instance, all "name of periodic table's group-bonding"-type, e.g., halogen, chalcogen, pnictogen, etc …, interactions, all require at least an atom of the specified type, among other conditions).

Lastly, not only high explosives were obtained, but we managed to elucidate an intimate (linear for what concerns E_a and logA, exponential for k) relationship among molecular extent of picrate-picrate contacts and thermal stability of **1**–**4** high-energy compounds. This level of detail, to the best of our knowledge, is unprecedented, and probably made possible through the use of structurally closely related (homologous) ligands. We hope that this piece of information will be of use in the development and engineering of "safe to handle", so to speak, detonating materials.

Limitations of the study

This study reports an experimental correlation between structural and thermokinetical parameters. Any correlation between explosive sensitivity and its structure is clearly of high pragmatic interest to strike a balance between energy content and safety of use of high-energy material. The present case is plainly a case study involving only 4 solid state complexes: this is an obvious limitation to its generality. Still, it is also the first time that such a clear correlation is drawn.

We suspect that full appreciation of found existing trend has been made possible by working with a series of homologous ligands forming same stoichiometry complexes with an overall homogeneity of interactions and for which both complete structural and thermochemical data are available: this is not a frequent case. This does not reduce the importance of having appreciated a correlation, as we made progress toward identifying and quantifying structure-properties relationship for high-energy materials.

Extension of herein-developed concepts to further experimental cases seems a strong suggestion, in theory. In practice, this requires the synthesis, crystallization, and structural determination of novel picrate-based classes of high explosives, verification of homogeneousness of the nature of packing interactions among chosen class (to tune down other potentially interfering factors), and determination of their thermokinetic properties (please read: heating high explosives).

Considering regulations and inherent hazards, we consider already a feat to have managed to show structure-properties correlation in our, arguably small, dataset.

STAR★METHODS

Detailed methods are provided in the online version of this paper and include the following:

- KEY RESOURCES TABLE
- RESOURCE AVAILABILITY
  - Lead contact
  - Materials availability
  - Data and code availability
- METHOD DETAILS
  - Caution statement
  - Materials
  - Synthesis of $H_2Lx(Picr)_2$
  - X-Ray structure analyses
  - Potentiometric measurements
  - Thermal analysis
  - Calculated heats of formation
  - Density functional theory calculation
  - Hirshfeld surface analysis
- QUANTIFICATION AND STATISTICAL ANALYSIS

SUPPLEMENTAL INFORMATION

Supplemental information can be found online at https://doi.org/10.1016/j.isci.2023.107330.

ACKNOWLEDGMENTS

The financial support provided by the MUR - Dipartimenti di Eccellenza 2023–2027 (DICUS 2.0) to the Department of Chemistry "Ugo Schiff" of the University of Florence is acknowledged.

AUTHOR CONTRIBUTIONS

Conceptualization: M.S., C.B., M.M., A.B.; Methodology: M.S., M.D.L., M.P., F.R., C.B.; Validation: M.P., G.P., C.B., A.B., Formal analysis: M.S., M.P., G.P., F.R., C.B.; Investigation: M.D.L., M.S., M.P., G.P.; Resources: M.D.L., M.P., F.R., M.M.; Writing – Original Draft: M.S., M.P., F.R., C.B., M.M.; Writing – Review & Editing: all authors; Visualization: M.S., C.B., A.B; Supervision: M.M., A.B.

DECLARATION OF INTERESTS

The authors declare no competing interests.

Received: June 22, 2023
Revised: June 27, 2023
Accepted: July 5, 2023
Published: July 10, 2023

REFERENCES

1. Fershtat, L.L. (2023). Recent advances in the synthesis and performance of 1,2,4,5-tetrazine-based energetic materials. FirePhysChem *3*, 78–87. https://doi.org/10.1016/j.fpc.2022.09.005.

2. O'Sullivan, O.T., and Zdilla, M.J. (2020). Properties and Promise of Catenated Nitrogen Systems As High-Energy-Density Materials. Chem. Rev. *120*, 5682–5744. https://doi.org/10.1021/acs.chemrev.9b00804.

3. De La Garza, G.D., Kaur, A.P., Shkrob, I.A., Robertson, L.A., Odom, S.A., and McNeil, A.J. (2022). Soluble and stable symmetric tetrazines as anolytes in redox flow batteries. J. Mater. Chem. A Mater. *10*, 18745–18752. https://doi.org/10.1039/D2TA04515J.

4. Masson, G., Lyu, J., Clémence, Claraz, A., Masson, G., Audebert, P., and Le. (2021). s-Tetrazine: Robust and Green Photoorganocatalyst for Aerobic Oxidation of N,N-Disubstituted Hydroxylamines to Nitrones. Synlett *33*, 177–181. https://doi.org/10.1055/a-1691-0449.

5. Razavi, S.A.A., Morsali, A., and Piroozzadeh, M. (2022). Redox Metal–Organic Framework for Photocatalytic Organic Transformation: The Role of Tetrazine Function in Radical-Anion Pathway. Inorg. Chem. *61*, 19134–19143. https://doi.org/10.1021/acs.inorgchem.2c02733.

6. Lerma-Berlanga, B., Ganivet, C.R., Almora-Barrios, N., Vismara, R., Navarro, J.A.R., Tatay, S., Padial, N.M., and Martí-Gastaldo, C. (2022). Tetrazine Linkers as Plug-and-Play Tags for General Metal-Organic Framework Functionalization and C60 Conjugation. Angew. Chem. Int. Ed. Engl. *61*, e202208139. https://doi.org/10.1002/anie.202208139.

7. Joshi, S., Raj, K.A., Rao, M.R., and Ghosh, R. (2022). An electronic biosensor based on semiconducting tetrazine polymer immobilizing matrix coated on rGO for carcinoembryonic antigen. Sci. Rep. *12*, 3006. https://doi.org/10.1038/s41598-022-06976-0.

8. K, A.R., Joshi, S., Ghosh, R., and Rajeswara Rao, M. (2023). Structural tailoring of semiconducting tetrazine polymers based immobilizing matrix for superior electronic biosensing of carcinoembryonic antigen. Polym. Adv.Technol. https://doi.org/10.1002/pat.5973.

9. Mavragani, N., Errulat, D., Gálico, D.A., Kitos, A.A., Mansikkamäki, A., and Murugesu, M. (2021). Radical-Bridged Ln4 Metallocene Complexes with Strong Magnetic Coupling and a Large Coercive Field. Angew. Chem. Int. Ed. Engl. *60*, 24206–24213. https://doi.org/10.1002/anie.202110813.

10. Mavragani, N., Kitos, A.A., Mansikkamäki, A., and Murugesu, M. (2023). New members of radical bridged Ln2 metallocene single-molecule magnets based on the unsubstituted 1,2,4,5-tetrazine ligand. Inorg. Chem. Front. *10*, 259–266. https://doi.org/10.1039/D2QI02164A.

11. Zhang, J., Shukla, V., and Boger, D.L. (2019). Inverse Electron Demand Diels–Alder Reactions of Heterocyclic Azadienes, 1-Aza-1,3-Butadienes, Cyclopropenone Ketals, and Related Systems. A Retrospective. J. Org. Chem. *84*, 9397–9445. https://doi.org/10.1021/acs.joc.9b00834.

12. Wu, H., and Devaraj, N.K. (2018). Advances in Tetrazine Bioorthogonal Chemistry Driven by the Synthesis of Novel Tetrazines and Dienophiles. Acc. Chem. Res. *51*, 1249–1259. https://doi.org/10.1021/acs.accounts.8b00062.

13. Deb, T., Tu, J., and Franzini, R.M. (2021). Mechanisms and Substituent Effects of Metal-Free Bioorthogonal Reactions. Chem. Rev. *121*, 6850–6914. https://doi.org/10.1021/acs.chemrev.0c01013.

14. Jemas, A., Xie, Y., Pigga, J.E., Caplan, J.L., am Ende, C.W., and Fox, J.M. (2022). Catalytic Activation of Bioorthogonal Chemistry with Light (CABL) Enables Rapid, Spatiotemporally Controlled Labeling and No-Wash, Subcellular 3D-Patterning in Live Cells Using Long Wavelength Light. J. Am. Chem. Soc. *144*, 1647–1662. https://doi.org/10.1021/jacs.1c10390.

15. Wheeler, S.E., and Bloom, J.W.G. (2014). Anion–π interactions and positive electrostatic potentials of N-heterocycles arise from the positions of the nuclei, not changes in the π-electron distribution. Chem. Commun. *50*, 11118–11121. https://doi.org/10.1039/C4CC05304D.

16. Savastano, M., García-Gallarín, C., López de la Torre, M.D., Bazzicalupi, C., Bianchi, A., and Melguizo, M. (2019). Anion-π and lone pair-π interactions with s-tetrazine-based ligands. Coord. Chem. Rev. *397*, 112–137. https://doi.org/10.1016/j.ccr.2019.06.016.

17. Schottel, B.L., Chifotides, H.T., and Dunbar, K.R. (2008). Anion-π interactions. Chem. Soc. Rev. *37*, 68–83. https://doi.org/10.1039/B614208G.

18. Chifotides, H.T., and Dunbar, K.R. (2013). Anion−π Interactions in Supramolecular Architectures. Acc. Chem. Res. *46*, 894–906. https://doi.org/10.1021/ar300251k.

19. Zhao, Y., Li, Y., Qin, Z., Jiang, R., Liu, H., and Li, Y. (2012). Selective and colorimetric fluoride anion chemosensor based on

s-tetrazines. Dalton Trans. *41*, 13338–13342. https://doi.org/10.1039/C2DT31641B.

20. Campos-Fernández, C.S., Schottel, B.L., Chifotides, H.T., Bera, J.K., Bacsa, J., Koomen, J.M., Russell, D.H., and Dunbar, K.R. (2005). Anion Template Effect on the Self-Assembly and Interconversion of Metallacyclophanes. J. Am. Chem. Soc. *127*, 12909–12923. https://doi.org/10.1021/ja052108q.

21. Chifotides, H.T., Giles, I.D., and Dunbar, K.R. (2013). Supramolecular Architectures with π-Acidic 3,6-Bis(2-pyridyl)-1,2,4,5-tetrazine Cavities: Role of Anion−π Interactions in the Remarkable Stability of Fe(II) Metallacycles in Solution. J. Am. Chem. Soc. *135*, 3039–3055. https://doi.org/10.1021/ja3082473.

22. Schottel, B.L., Chifotides, H.T., Shatruk, M., Chouai, A., Pérez, L.M., Bacsa, J., and Dunbar, K.R. (2006). Anion−π Interactions as Controlling Elements in Self-Assembly Reactions of Ag(I) Complexes with π-Acidic Aromatic Rings. J. Am. Chem. Soc. *128*, 5895–5912. https://doi.org/10.1021/ja0606273.

23. Guo, Q.-H., Fu, Z.-D., Zhao, L., and Wang, M.-X. (2014). Synthesis, Structure, and Properties of O6-Corona[3]arene[3]tetrazines. Angew. Chem. Int. Ed. Engl. *53*, 13548–13552. https://doi.org/10.1002/anie.201407670.

24. Liu, H.-B., Zhang, Q., and Wang, M.-X. (2018). Synthesis, Structure, and Anion Binding Properties of Electron-Deficient Tetrahomocorona[4]arenes: Shape Selectivity in Anion–π Interactions. Angew. Chem. Int. Ed. Engl. *57*, 6536–6540. https://doi.org/10.1002/anie.201802650.

25. Savastano, M., Bazzicalupi, C., Giorgi, C., García-Gallarín, C., López de la Torre, M.D., Pichierri, F., Bianchi, A., and Melguizo, M. (2016). Anion Complexes with Tetrazine-Based Ligands: Formation of Strong Anion−π Interactions in Solution and in the Solid State. Inorg. Chem. *55*, 8013–8024. https://doi.org/10.1021/acs.inorgchem.6b01138.

26. Savastano, M., García-Gallarín, C., Giorgi, C., Gratteri, P., López de la Torre, M.D., Bazzicalupi, C., Bianchi, A., and Melguizo, M. (2019). Solid State and Solution Study on the Formation of Inorganic Anion Complexes with a Series of Tetrazine-Based Ligands. Molecules *24*, 2247. https://doi.org/10.3390/molecules24122247.

27. Savastano, M., Bazzicalupi, C., García, C., Gellini, C., López de la Torre, M.D., Mariani, P., Pichierri, F., Bianchi, A., and Melguizo, M. (2017). Iodide and triiodide anion complexes involving anion–π interactions with a tetrazine-based receptor. Dalton Trans. *46*, 4518–4529. https://doi.org/10.1039/C7DT00134G.

28. Savastano, M., García, C., López de la Torre, M.D., Pichierri, F., Bazzicalupi, C., Bianchi, A., and Melguizo, M. (2018). Interplay between salt bridge, hydrogen bond and anion-π interactions in thiocyanate binding. Inorg. Chim. Acta. *470*, 133–138. https://doi.org/10.1016/j.ica.2017.04.029.

29. Savastano, M., Bazzicalupi, C., García-Gallarín, C., Giorgi, C., López de la Torre, M.D., Pichierri, F., Bianchi, A., and Melguizo, M. (2018). Halide and hydroxide anion binding in water. Dalton Trans. *47*, 3329–3338. https://doi.org/10.1039/C7DT04430E.

30. Savastano, M., Bazzicalupi, C., García-Gallarín, C., López de la Torre, M.D., Bianchi, A., and Melguizo, M. (2019). Supramolecular forces and their interplay in stabilizing complexes of organic anions: tuning binding selectivity in water. Org. Chem. Front. *6*, 75–86. https://doi.org/10.1039/C8QO01152D.

31. Savastano, M., Bazzicalupi, C., Mariani, P., and Bianchi, A. (2018). Network Formation via Anion Coordination: Crystal Structures Based on the Interplay of Non-Covalent Interactions. Molecules *23*, 572. https://doi.org/10.3390/molecules23030572.

32. Egli, M., and Sarkhel, S. (2007). Lone Pair−Aromatic Interactions: To Stabilize or Not to Stabilize. Acc. Chem. Res. *40*, 197–205. https://doi.org/10.1021/ar068174u.

33. Jain, A., Ramanathan, V., and Sankararamakrishnan, R. (2009). Lone pair ··· π interactions between water oxygens and aromatic residues: Quantum chemical studies based on high-resolution protein structures and model compounds. Protein Sci. *18*, 595–605. https://doi.org/10.1002/pro.67.

34. Lu, Z., Gamez, P., Mutikainen, I., Turpeinen, U., and Reedijk, J. (2007). Supramolecular Assemblies Generated from Both Lone-Pair···π and C−H···π Binding Interactions. Cryst. Growth Des. *7*, 1669–1671. https://doi.org/10.1021/cg0704302.

35. Mooibroek, T.J., Gamez, P., and Reedijk, J. (2008). Lone pair–π interactions: a new supramolecular bond? CrystEngComm *10*, 1501–1515. https://doi.org/10.1039/B812026A.

36. Sarkhel, S., Rich, A., and Egli, M. (2003). Water−Nucleobase "Stacking": H−π and Lone Pair−π Interactions in the Atomic Resolution Crystal Structure of an RNA Pseudoknot. J. Am. Chem. Soc. *125*, 8998–8999. https://doi.org/10.1021/ja0357801.

37. Bauzá, A., Mooibroek, T.J., and Frontera, A. (2015). The Bright Future of Unconventional σ/π-Hole Interactions. ChemPhysChem *16*, 2496–2517. https://doi.org/10.1002/cphc.201500314.

38. Groom, C.R., Bruno, I.J., Lightfoot, M.P., and Ward, S.C. (2016). The Cambridge Structural Database. Acta Cryst B *72*, 171–179. https://doi.org/10.1107/S2052520616003954.

39. Bu, R., Xiong, Y., and Zhang, C. (2020). π–π Stacking Contributing to the Low or Reduced Impact Sensitivity of Energetic Materials. Cryst. Growth Des. *20*, 2824–2841. https://doi.org/10.1021/acs.cgd.0c00367.

40. Dosch, D.E., Reichel, M., Born, M., Klapötke, T.M., and Karaghiosoff, K. (2021). Investigation of Structure–Property Relationships of Three Nitroaromatic Compounds: 1-Fluoro-2,4,6-trinitrobenzene, 2,4,6-Trinitrophenyl Methanesulfonate, and 2,4,6-Trinitrobenzaldehyde. Cryst. Growth Des. *21*, 243–248. https://doi.org/10.1021/acs.cgd.0c01049.

41. Bu, R., Xie, W., and Zhang, C. (2019). Heat-Induced Polymorphic Transformation Facilitating the Low Impact-Sensitivity of 2,2-Dinitroethylene-1,1-diamine (FOX-7). J. Phys. Chem. C *123*, 16014–16022. https://doi.org/10.1021/acs.jpcc.9b03921.

42. Zhang, C., Jiao, F., and Li, H. (2018). Crystal Engineering for Creating Low Sensitivity and Highly Energetic Materials. Cryst. Growth Des. *18*, 5713–5726. https://doi.org/10.1021/acs.cgd.8b00929.

43. Zhang, B., Wu, X., Wang, X., Li, S., Ma, J., Liao, G., Li, Y., Zhang, J., Zhang, J., and Shreeve, J.M. (2022). Synthesis of a high-energy-density material through rapid replacement of crystal water of hydrates. Chem *47*, 2678–2681. https://doi.org/10.1016/j.chempr.2022.06.007.

44. Garau, C., Quiñonero, D., Frontera, A., Costa, A., Ballester, P., and Deyà, P.M. (2003). s-Tetrazine as a new binding unit in molecular recognition of anions. Chem. Phys. Lett. *370*, 7–13. https://doi.org/10.1016/S0009-2614(03)00020-4.

45. Arranz-Mascarós, P., Bazzicalupi, C., Bianchi, A., Giorgi, C., Godino-Salido, M.-L., Gutiérrez-Valero, M.D., Lopez-Garzón, R., and Savastano, M. (2013). Thermodynamics of Anion−π Interactions in Aqueous Solution. J. Am. Chem. Soc. *135*, 102–105. https://doi.org/10.1021/ja311389z.

46. Martínez-Camarena, Á., Savastano, M., Bazzicalupi, C., Bianchi, A., and García-España, E. (2020). Stabilisation of Exotic Tribromide (Br3−) Anions via Supramolecular Interaction with A Tosylated Macrocyclic Pyridinophane. Molecules *25*, 3155. https://doi.org/10.3390/molecules25143155.

47. Zhou, T., Zybin, S.V., Liu, Y., Huang, F., and Goddard, W.A. (2012). Anisotropic shock sensitivity for β-octahydro-1,3,5,7-tetranitro-1,3,5,7-tetrazocine energetic material under compressive-shear loading from ReaxFF-lg reactive dynamics simulations. J. Appl. Phys. *111*, 124904. https://doi.org/10.1063/1.4729114.

48. Macrae, C.F., Sovago, I., Cottrell, S.J., Galek, P.T.A., McCabe, P., Pidcock, E., Platings, M., Shields, G.P., Stevens, J.S., Towler, M., and Wood, P.A. (2020). Mercury 4.0: from visualization to analysis, design and prediction. J Appl Cryst *53*, 226–235. https://doi.org/10.1107/S1600576719014092.

49. Zhou, J., Ding, L., Bi, F., Wang, B., and Zhang, J. (2018). Research on the thermal behavior of novel heat resistance explosive 5,5′-bis(2,4,6-trinitrophenyl)-2,2′-bi(1,3,4-oxadiazole). J. Anal. Appl. Pyrol. *129*, 189–194. https://doi.org/10.1016/j.jaap.2017.11.013.

50. Zhang, B., and Liu, S.-H. (2020). Thermal stability assessment of 4-amino-1,2,4-triazole picrate using thermal analysis method. J. Therm. Anal. Calorim. *139*, 2155–2163. https://doi.org/10.1007/s10973-019-08614-w.

51. Thermochemical Computer Code EXPLO5 Thermochemical Computer Code EXPLO5. https://www.ozm.cz/explosives-performance-tests/thermochemical-computer-code-explo5/.

52. Bruker (2001 (Bruker AXS Inc), SAINT.

53. Sheldrick, G.M. (2008). A short history of SHELX. Acta Cryst A *64*, 112–122. https://doi.org/10.1107/S0108767307043930.

54. Sheldrick, G.M. (2015). Crystal structure refinement with SHELXL. Acta Cryst C *71*, 3–8. https://doi.org/10.1107/S2053229614024218.

55. Savastano, M., Bazzicalupi, C., Ferraro, G., Fratini, E., Gratteri, P., and Bianchi, A. (2019). Tales of the Unexpected: The Case of Zirconium(IV) Complexes with Desferrioxamine. Molecules *24*, 2098. https://doi.org/10.3390/molecules24112098.

56. Fontanelli, M., and Micheloni, M. (1990). In Proceedings of the I Spanish-Italian Congress on Thermodynamics of Metal Complexes (Diputación de Castellón), pp. 41–43.

57. Savastano, M., Fiaschi, M., Ferraro, G., Gratteri, P., Mariani, P., Bianchi, A., and Bazzicalupi, C. (2020). Sensing Zn2+ in Aqueous Solution with a Fluorescent Scorpiand Macrocyclic Ligand Decorated with an Anthracene Bearing Tail. Molecules *25*, 1355. https://doi.org/10.3390/molecules25061355.

58. Gran, G. (1952). Determination of the equivalence point in potentiometric titrations. Part II. Analyst *77*, 661–671. https://doi.org/10.1039/AN9527700661.

59. Gans, P., Sabatini, A., and Vacca, A. (1996). Investigation of equilibria in solution. Determination of equilibrium constants with the HYPERQUAD suite of programs. Talanta *43*, 1739–1753. https://doi.org/10.1016/0039-9140(96)01958-3.

60. Wu, J.-T., Zhang, J.-G., Yin, X., Cheng, Z.-Y., and Xu, C.-X. (2015). 3,4-Diamino-1,2,4-triazole based energetic salts: synthesis, characterization, and energetic properties. New J. Chem. *39*, 5265–5271. https://doi.org/10.1039/C5NJ00182J.

61. Zhang, J., and Xiao, H. (2002). Computational studies on the infrared vibrational spectra, thermodynamic properties, detonation properties, and pyrolysis mechanism of octanitrocubane. J. Chem. Phys. *116*, 10674–10683. https://doi.org/10.1063/1.1479136.

62. Liu, T., Liao, S., Song, S., Wang, K., Jin, Y., and Zhang, Q. (2019). Combination of gem-dinitromethyl functionality and a 5-amino-1,3,4-oxadiazole framework for zwitterionic energetic materials. Chem. Commun. *56*, 209–212. https://doi.org/10.1039/C9CC08182H.

63. Zhao, Y., and Truhlar, D.G. (2008). The M06 suite of density functionals for main group thermochemistry, thermochemical kinetics, noncovalent interactions, excited states, and transition elements: two new functionals and systematic testing of four M06-class functionals and 12 other functionals. Theor. Chem. Acc. *120*, 215–241. https://doi.org/10.1007/s00214-007-0310-x.

64. Dunning, T.H. (1989). Gaussian basis sets for use in correlated molecular calculations. I. The atoms boron through neon and hydrogen. J. Chem. Phys. *90*, 1007–1023. https://doi.org/10.1063/1.456153.

65. Lemoult, M.P. (1907). Recherches theoriques et experimentales sur les chaleurs de combustion et de formation des composes organiques. Ann. Chim. Phys. *12*, 395–432.

66. Liu, Z., Wu, Q., Zhu, W., and Xiao, H. (2013). Theoretical study of energetic trinitromethyl-substituted tetrazole and tetrazine derivatives. J. Phys. Org. Chem. *26*, 939–947. https://doi.org/10.1002/poc.3197.

67. Chase, M.W. (1998). NIST-JANAF Thermochemical Tables, 4th Edition (American Institute of Physics (M W. Chase)).

68. Manion, J.A. (2002). Evaluated Enthalpies of Formation of the Stable Closed Shell C1 and C2 Chlorinated Hydrocarbons. J. Phys. Chem. Ref. Data *31*, 123–172. https://doi.org/10.1063/1.1420703.

69. Kabli, S., van Beelen, E.S., Ingemann, S., Henriksen, L., and Hammerum, S. (2006). The proton affinities of saturated and unsaturated heterocyclic molecules. Int. J. Mass Spectrom. *249–250*, 370–378. https://doi.org/10.1016/j.ijms.2005.11.021.

70. Jenkins, H.D.B., Tudela, D., and Glasser, L. (2002). Lattice Potential Energy Estimation for Complex Ionic Salts from Density Measurements. Inorg. Chem. *41*, 2364–2367. https://doi.org/10.1021/ic011216k.

71. Benson, S.W., and Buss, J.H. (1958). Additivity Rules for the Estimation of Molecular Properties. Thermodynamic Properties. J. Chem. Phys. *29*, 546–572. https://doi.org/10.1063/1.1744539.

72. Frisch, M.J., Trucks, G.W., Schlegel, H.B., Scuseria, G.E., Robb, M.A., Cheeseman, J.R., Scalmani, G., Barone, V., Mennucci, B., Petersson, G.A., et al. (2010). Gaussian 09, Revision C.01 (Gaussian, Inc).

73. Spackman, M.A., and Byrom, P.G. (1997). A novel definition of a molecule in a crystal. Chem. Phys. Lett. *267*, 215–220. https://doi.org/10.1016/S0009-2614(97)00100-0.

74. McKinnon, J.J., Spackman, M.A., and Mitchell, A.S. (2004). Novel tools for visualizing and exploring intermolecular interactions in molecular crystals. Acta Cryst B *60*, 627–668. https://doi.org/10.1107/S0108768104020300.

75. Spackman, M.A., and McKinnon, J.J. (2002). Fingerprinting intermolecular interactions in molecular crystals. CrystEngComm *4*, 378–392. https://doi.org/10.1039/B203191B.

76. Spackman, P.R., Turner, M.J., McKinnon, J.J., Wolff, S.K., Grimwood, D.J., Jayatilaka, D., and Spackman, M.A. (2021). CrystalExplorer: a program for Hirshfeld surface analysis, visualization and quantitative analysis of molecular crystals. J Appl Cryst *54*, 1006–1011. https://doi.org/10.1107/S1600576721002910.

STAR★METHODS

KEY RESOURCES TABLE

REAGENT or RESOURCE	SOURCE	IDENTIFIER
Chemicals, peptides, and recombinant proteins		
L1 (3,6-bis(morpholinomethyl)-1,2,4,5-tetrazine)	M. Melguizo et al.[25]	N/A
L2 (3,6-bis(2-morpholinoethyl)-1,2,4,5-tetrazine)	M. Melguizo et al.[25]	N/A
L3 (3,6-bis(3-morpholinopropyl)-1,2,4,5-tetrazine)	M. Melguizo et al.[26]	N/A
L4 (3,6-bis(4-morpholinobutyl)-1,2,4,5-tetrazine)	M. Melguizo et al.[26]	N/A
Picric Acid solution	Sigma-Aldrich	CAS 88-89-1
NMe_4Cl	Sigma-Aldrich	CAS 75-57-0
Compounds **1-4**	This paper	N/A
Deposited data		
Compounds 1–4.cif files	This paper	CCDC: 2252946-2252949
Software and algorithms		
SAINT	Bruker[52]	https://www.bruker.com/en/products-and-solutions/diffractometers-and-x-ray-microscopes/single-crystal-x-ray-diffractometers/sc-xrd-software/apex.html
SHELXS-97	G. M. Sheldrick[53]	https://doi.org/10.1107/S0108767307043930
SHELXL Version 2014/7.	G. M. Sheldrick[54]	https://doi.org/10.1107/S2053229614024218
PASAT	M. Fontanelli, M. Micheloni[56]	N/A – Please contact original authors
HYPERQUAD	Gans, P. et al.	http://www.hyperquad.co.uk/HQ2013.htm
Gaussian 09	M. J. Frisch et al.[72]	https://gaussian.com
CrystalExplorer21	P. R. Spackman et al.[76]	https://crystalexplorer.net/
CCDC Mercury	C. F. Macrae et al.[48]	https://www.ccdc.cam.ac.uk/solutions/software/mercury/
EXPLO5	M. Suceska, OZM research[51]	https://www.ozm.cz/explosives-performance-tests/thermochemical-computer-code-explo5/

RESOURCE AVAILABILITY

Lead contact

Further information and requests for resources should be directed to and will be fulfilled by the lead contact, Matteo Savastano (matteo.savastano@uniroma5.it).

Materials availability

All materials generated in this study can be obtained according to the described methods. Direct availability of $[H_2L(picrate)_2]$ complexes (L = L1-L4) from the authors is limited due to intrinsic explosion hazard.

Data and code availability

- The accession number for the crystal structures reported in this paper is CCDC: 2252946-2252949.
- This paper does not report original code.

- Any additional information required to reanalyze the data reported in this paper is available from the lead contact upon request.

METHOD DETAILS

Caution statement

Caution! Picric acid is explosive and should be handled safely and in small quantities. Aqueous solutions are relatively safe. Contamination with metals should be avoided. Derivatives of s-tetrazine might be explosive and should be handled carefully in small quantities. Synthesis of explosive substances or their mixing with further potentially explosive substances should also be done safely and in very small quantities. Heating of explosive/potentially explosive materials is dangerous and generally not advisable. No issues were encountered during this study.

Materials

L1-L4 were synthetized as previously described.[25,26] Employed water was of MilliQ grade. NMe_4Cl, employed as ionic strength in potentiometric measurements, was purchased as solid salt from Sigma Aldrich. Picric acid was purchased as its saturated aqueous solution from the same supplier. When solid samples of it were needed, they were obtained by cooling a small volume of its saturated solution and then recovering picric acid crystals from it.

Synthesis of $H_2Lx(Picr)_2$

$H_2Lx(Picr)_2$ salts can be obtained quantitatively by mixing L1-L4 ligands (pink) with excess picric acid (as saturated picric acid solution) (yellow) in water in small volume: fast precipitation of orange $H_2Lx(Picr)_2$ is observed: the process is quantitative and signaled by the solution regaining the yellow tone of free picric acid. Precipitation can instead be avoided/postponed by working in dilute conditions and/or sub-stoichiometric L:Picr ratio (see potentiometric measurements section).

Single crystals of $H_2Lx(Picr)_2$ compounds were instead obtained by diffusion-type experiments.

In a typical experiment, 20 mg of Lx (x = 1–4) are put on one side of an H-shaped tube (≈10 mL volume) together with a few drops of HCl 0.1 M (to promote ligand dissolution and diffusion). On the other side of the tube, saturated picric acid solution is placed. The tube is then filled with water so that diffusing Lx and picric acid may come in contact. Single crystals are then slowly formed over days or weeks, depending on the solubility of the complexes, which also affects global yields. Under our conditions, experimental yields are: $H_2L1(Picr)_2$(**1**): 76.2%; $H_2L2(Picr)_2$(**2**): 39.9%; $H_2L3(Picr)_2$ (**3**): 82.2%; $H_2L4(Picr)_2$ (**4**): 42.3%.

X-Ray structure analyses

Orange crystals of $H_2L(picrate)_2$ (L = L1 (**1**), L2 (**2**) and L3(**3**)) and red crystals of $H_2L4(picrate)_2$ (**4**) were used for X-ray diffraction analysis. A summary of the crystallographic data is reported in Table S1. The integrated intensities were corrected for Lorentz and polarization effects and an empirical absorption correction was applied.[52] The structures were solved by direct methods (SHELXS-97).[53] Refinements were performed by means of full-matrix least-squares using SHELXL Version 2014/7.[54] All the non-hydrogen atoms were anisotropically refined. Hydrogen atoms were usually introduced in calculated position and their coordinates were refined according to the linked atoms. The acidic hydrogens in (**1**), (**2**) and (**3**) were localized in the corresponding Fourier difference maps, introduced in the calculation and freely refined.

Potentiometric measurements

Potentiometric (pH-metric) titrations, for the determination of the equilibrium constants were performed in 0.1 M Me_4NCl at 298.1 ± 0.1 K using an automated apparatus and a procedure that has been previously described (Supplementary materials of ref. 55). The acquisition of the emf data was performed with the computer program PASAT.[56,57] A combined electrode (Metrohm 6.0262.100, Metrohm, Herisau, Switzerland) was calibrated as a hydrogen-ion concentration probe through the titration of standardized HCl solutions with standardized CO_2-free NaOH solutions and by determining the equivalent point using Gran's method,[58] which furnishes the standard potential (E°) and the ionic product of water (pK_w = 13.83(1) in 0.1 M Me_4NCl at 298.1 K). The HYPERQUAD[59] computer program was employed to calculate the stability constants from potentiometric data.

Stable L:picrate solutions, i.e., not affected by precipitation phenomena over the time frame required for potentiometric titrations, must be obtained. Concentrations should also be in an accessible range for the technique. This is not possible for L1 and L3, due to high insolubility of $H_2L(Picr)_2$. L2 and L4 can instead be titrated with [L] = 1 mM and [Picr]/[L] up to 2.0.

Thermal analysis

The analysis was conducted with a TA Instruments SDT Q650 (TA Instruments, New Castle, DE, USA), which allows for the simultaneous monitoring of the weight loss signal (TGA curve and its derivative, i.e., DTG curve) and the heat flow profile (DSC curve). Samples were placed in an alumina pan and measured in N_2 atmosphere (flow rate 100 mL/min) from room temperature to 600°C. Thermal profiles of ligands (L1/L4) and picric acid (PA) were acquired at 10°C/min, while those of compounds 1–4 were recorded at 5°C/min, 10 °C/min, 20 °C/min and 50 °C/min. The use of a simultaneous TGA/DSC apparatus enabled to test the materials in a safe mode, using little amounts of materials, with short analyses, which give simultaneously two significant information (weight loss and heat flow).

Calculated heats of formation

The heat of formation for the $H_2L1(picrate)_2$ salt was calculated based on the following Born-Haber cycle (Scheme 1).

$$\Delta H_f^\circ\left(H_2L1\left(picrate\right)_2, 298\ K\right) = \Delta H_f^0\left(H_2L1^{2+}, 298\ K\right) + 2\Delta H_f^0\left(picrate, 298\ K\right) - \Delta H_L$$

where ΔH_f°(picrate, 298 K) was taken from Table 2 (ΔH_f anion column) of ref.,[60] ΔH_L depends on the lattice-potential energy and $\Delta H_f^0(H_2L1^{2+})$ can be calculated by the isodesmic reaction method.[61,62]

The suitable isodesmic reaction is:

$$H_2L1^{2+} + 2NH_3 + 2CH_4 \rightarrow 2Hmorfoline^+ + tetrazine + 2CH_3 - CH_2 - NH_2$$

The ΔH_{reaz}° for the isodesmic reaction can be calculated by each one of the following equations:

$$\Delta H_{reaz}^\circ\ (298\ K) = \Sigma\ (E_0+H_{corr})_{products} - \Sigma\ (E_0+H_{corr})_{reactants} \qquad \text{(Equation 1)}$$

and

$$\Delta H_{reaz}^\circ\ (298\ K) = \Sigma\ \Delta H_{f\,products}^\circ - \Sigma\ \Delta H_{f\,reactant}^\circ \qquad \text{(Equation 2)}$$

In Equation 1, E_0 are the M062X/cc-pVTZ gas phase energy at 0 K,[63,64] added of the zero-point energy and thermal factors up to 298 K (all reactants and products were optimized and characterized as true local minima on the potential-energy surface by frequence analysis; input coordinates for H_2L1^{2+} taken from the $H_{Equation\ 2}L1(picrate)_2$ crystal structure).

In 2 all data are known from literature with the exception of ΔH_{reaz}^0 and the heat of formation of the diprotonated ligand L1. Thus, by equating Equations 1 and 2, the unknown $\Delta H_f^0(H_2L1^{2+})$ can be calculated.

Used reference values are as follows: Ethylamine: −57.7 kJ/mol,[65]; *s*-tetrazine: 482.62 kJ/mol,[66]; NH_3:-45.9 kJ/mol,[67]; CH_4:-74.9 kJ/mol,[68]; protonated morpholine: 461 kJ/mol.[69]

Concerning the ΔH_L value, as stated above it depends on the lattice-potential energy. Actually, as both anion and cation in $H_2L1(picrate)_2$ are non-linear polyatomic species, ΔH_L is given by the Equation 3.

$$\Delta H_L\ (kJ\ mol^{-1}) = Upot\ (kJ\ mol^{-1}) + [(6/2-2) + 2(6/2-2)]RT \qquad \text{(Equation 3)}$$

and Upot can be calculated from the density of the crystalline material by using Equation 4.

$$Upot\ (kJ\ mol^{-1}) = \gamma[(\rho_{calc}/1.66)/Mw]^{1/3} + \delta \qquad \text{(Equation 4)}$$

where ρ_{calc} is the calculated density (g/cm^3) of the crystal structure, Mw is the compound's molar mass (g/mol) and γ and δ are tabulated parameters depending on the cation/anion stoichiometry ratio (γ = 6764.3 kJ and δ = 365.4 kJ for MX_2 salts).[70]

Once the heat of formation has been obtained for the first member of the series $H_2L1(picrate)_2$, the same quantity was obtained for all other members (L2, L3 and L4) by incremental method, adding the enthalpic contribution of two CH_2 groups.[71]

All calculated values are reported in Table S3.

Density functional theory calculation

Density functional theory (DFT) calculations have been carried out with Gaussian 09 suite of programs[72] at M06-2x/cc-pVTZ level of theory.[63,64] All the molecular structures have been optimized with very tight criterium, using an ultrafine grid; vibrational frequencies have been computed to assert that a true minimum has been located and it has been verified that all the vibrational frequencies were real. This first result is particularly important for subsequent thermodynamic analysis.

Hirshfeld surface analysis

Hirshfeld surface can be defined as enclosing the region of space where the electron density of the molecule under consideration (or more correctly of its promolecule) dominates the electron density of the crystal. The mathematical definition, properties and usefulness of the Hirshfeld surface are found in dedicated literature.[73,74] The same treatment allows for the visualization of a crystal structure through the lens of so-called fingerprint plots.[75] These are complete maps of external distance (d_e) (i.e., the point-by-point distance of the nearest atom belonging to another molecule to the Hirshfeld surface of considered species) vs. internal distance (d_i) (i.e., the point-by-point distance from a molecule's Hirshfeld surface and the nearest atom belonging to the molecule itself) from the Hirshfeld surface under consideration, are colour-coded to show relative abundance (from blue: few contacts, to red: many contacts) of intermolecular contacts occupying d_ixd_e square bins of 0.01 × 0.01 $Å^2$.

Hirshfeld surface and fingerprint plots were calculated using the Crystalexplorer21 software.[76]

Relevance of Hirshfeld approach to elucidation of high-energy material properties has been discussed elsewhere.[39,40]

QUANTIFICATION AND STATISTICAL ANALYSIS

Linear regression was used to extrapolate thermokinetics parameters from DSC data.

Used equation (Kissinger model) is described in the "thermal analysis of compounds 1–4" section.

Results of the fitting, including correlation coefficients are given in Table 5.

Plots of experimental data and resulting fit are given in Figure S8.